

Control of charge-spin interconversion in van der Waals heterostructures with chiral charge density waves

Zhendong Chi^{1*}, Seungjun Lee^{2*}, Haozhe Yang^{1*}, Eoin Dolan¹, C. K. Safeer^{1,3}, Josep Ingla-Aynés¹, Franz Herling¹, Nerea Ontoso¹, Beatriz Martín-García^{1,4}, Marco Gobbi^{4,5}, Tony Low^{2,6}, Luis E. Hueso^{1,4}, Fèlix Casanova^{1,4,†}

¹CIC nanoGUNE BRTA, 20018 Donostia-San Sebastián, Basque Country, Spain

²Department of Electrical and Computer Engineering, University of Minnesota, Minneapolis, Minnesota 55455, USA

³Department of Physics, Clarendon Laboratory, University of Oxford, OX13PU, Oxford, United Kingdom

⁴IKERBASQUE, Basque Foundation for Science, 48009 Bilbao, Basque Country, Spain

⁵Centro de Física de Materiales (CSIC-EHU/UPV) and Materials Physics Center (MPC), 20018 Donostia-San Sebastián, Basque Country, Spain

⁶Department of Physics, University of Minnesota, Minneapolis, Minnesota 55455, USA

*These authors equally contributed to this work.

†E-mail: f.casanova@nanogune.eu

ABSTRACT

A charge density wave (CDW) represents an exotic state in which electrons are arranged in a long range ordered pattern in low-dimensional materials. Although our understanding of the fundamental character of CDW has been enriched after extensive studies, its relationship with functional phenomena remains relatively limited. Here, we show an unprecedented demonstration of a tunable charge-spin interconversion (CSI) in graphene/1T-TaS₂ van der Waals heterostructures by manipulating the distinct CDW phases in 1T-TaS₂. Whereas CSI from spins polarized in all three directions are observed in the heterostructure when the CDW phase does not show commensurability, the output of one of the components disappears and the other two are enhanced when the CDW phase becomes commensurate. The experimental observation is supported by first-principles calculations, which evidence that chiral CDW multidomains are at the origin of the switching of CSI. Our results uncover a new approach for on-demand CSI in low-dimensional systems, paving the way for advanced spin-orbitronic devices.

1. Introduction

Efficient and controllable charge-spin interconversion (CSI) obtained in materials with strong spin-orbit coupling is crucial for novel spin-orbitronic applications, such as non-volatile memory [1] and logic devices [2] [3]. Conventional CSI effects include the spin Hall effect (SHE) in bulk materials [4] and the Rashba-Edelstein effect (REE) in two-dimensional systems with broken inversion symmetry [5]. By these mechanisms a spin current (j_s), in the former, or a spin density (n_s), in the latter, are generated by a charge current (j_c). Both effects obey reciprocity, leading to inverse effects with the same efficiency [6] [7]. In conventional materials with high symmetry, the directions of j_c and spin polarization (S) are perpendicular. Although large CSI values have been demonstrated in various systems [8] [9] [10] [11], controlling the CSI efficiency to design advanced multifunctional devices remains challenging.

Van der Waals materials, which have high electronic/structural tunability, provide a versatile platform for investigating novel spin-orbitronic phenomena [12]. Graphene (Gr) is an excellent van der Waals material for transferring spin current [13], but its weak spin-orbit coupling limits the generation of CSI. To overcome this issue, Gr can be combined with transition metal dichalcogenides (TMDCs) to form van der Waals heterostructures [14] [15] in which the strong spin-orbit coupling in the TMDC is imprinted onto Gr by proximity effect. Large CSI in Gr/TMDC heterostructures has been predicted [16] [17] [18] [19] and subsequently confirmed in experiments [20] [21] [22] [23]. An unconventional CSI, with j_c collinear to S , has been observed in some Gr/TMDC systems [24] [25] [26] [27] [28] and attributed to the broken mirror symmetries at the twisted interface [29] [30] [31] [32]. A remarkable characteristic of Gr/TMDC heterostructures is their tunable CSI efficiency by using a gate voltage to shift the Fermi level in Gr [21] [22]. However, controlling the CSI using the degrees of freedom in the TMDC counterpart has not yet been achieved.

The charge density wave (CDW), a long-range ordered state of electrons observed in low-dimensional materials including TMDC, exhibits a thermally activated modulation. Beyond its wide exploration for the fundamental connections with some correlated states of matter, such as unconventional superconductivity [33], its relationship with functional phenomena might be a promising direction. Here, we explore 1T-TaS₂, a TMDC featuring helical CDW phases with various degrees of commensurability [34, 35, 36], as an ideal platform for controlling CSI. By spin precession experiments, we confirm the CSI with the spins polarized in the three directions predicted in the twisted Gr/1T-TaS₂ heterostructure [32]. Furthermore, we observe the ON and OFF of the unconventional CSI component by tuning the commensurability of the CDW phase (Fig. 1a). Our first-principles calculations based on density functional theory reveal that the disappearance of the unconventional CSI arises from the presence of chiral CDW multidomain in the commensurate phase, where the sign of the CSI is locked to chirality. The rich interplay between proximity, commensurability, and chirality of the CDW in the Gr/1T-TaS₂ van der Waals heterostructures opens the path to tailor a plethora of spin-based phenomena in low-dimensional systems.

2. Results and Discussion

2.1 Gr/1T-TaS₂ heterostructure CSI devices

1T-TaS₂ undergoes a reversible incommensurate CDW (ICCDW) to nearly commensurate CDW (NCCDW) phase transition and a NCCDW to commensurate CDW (CCDW) phase transition by modulating the temperature [34], displaying a resistance hysteresis loop during a temperature sweep (Fig. 1b). In the CCDW phase, 1T-TaS₂ is filled with a star-of-David CDW lattice distortion from the normal state (Fig. 1a), exhibiting an insulating-like behavior. However, several tens of star-of-David CDW domains exist in the NCCDW phase while slight Ta-atom-position-shifts are observed in the ICCDW phase (see insets of Fig. 1b). The electrical transport in these two phases is thus limited by the normal metallic state [37]. The nature of the interfacial environment and transferred spin-orbit coupling from 1T-TaS₂ to Gr are contingent upon the CDW phase of 1T-TaS₂ [32]. Therefore, tunable CSI is expected in Gr/1T-TaS₂.

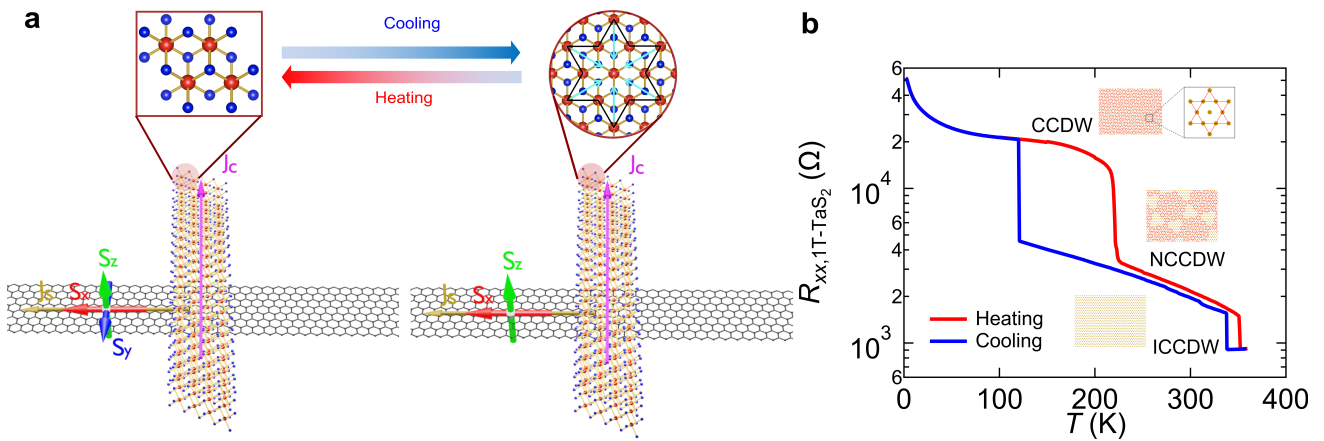


Figure 1. Graphene/1T-TaS₂ crystal structure and the charge-spin interaction. **a**, Schematic illustrations of charge-spin interconversion in graphene/1T-TaS₂ heterostructures in different 1T-TaS₂ phases. The spin polarization of the spin current (j_s , yellow arrow) along the x -, y -, and z -axes are labelled by red, blue, and green arrows. Top panel: top views of 1T-TaS₂ crystal structure in the normal (left) and CDW (right) states. The black lines in the sketch of the CDW state display the structure of the stars of David in 1T-TaS₂. The cyan arrows illustrate the distortion of the surrounding Ta atoms towards the central Ta atom. The middle arrows represent cooling (blue) and heating (red) cases. **b**, Temperature (T) dependent resistance of the 60-nm-thick 1T-TaS₂ nanocrystal ($R_{xx,1T-TaS_2}$) in Device 1 while cooling (blue) and heating (red). Inset: Formation of the stars of David in different CDW phases.

To thoroughly investigate the CSI in Gr/1T-TaS₂ heterostructures, we fabricated 3 different devices (see Methods and Supplementary Notes 1-3 for details on device fabrication and characterization). Figure 2a illustrates the measurement configuration of CSI. The device consists of a Gr/1T-TaS₂ Hall bar heterostructure, ferromagnetic (FM) electrodes, and non-magnetic (NM) electrodes. The FM electrodes are designed as elongated nanowires to obtain a magnetic easy axis along the y -axis. In our measurement, a dc charge current (I_{dc}) is applied across the 1T-TaS₂ layer. In the presence of CSI in the heterostructure, the charge current is converted into a spin current which diffuses in Gr along the x -axis while keeping its spin polarization (S_x , S_y , and S_z shown in Fig. 2a). Such spin current generates

a non-local voltage (V_{NL}) at the FM/Gr interface, which we detect between the FM and NM electrodes on Gr. The non-local CSI resistance is defined as $R_{NL} = V_{NL}/I_{dc}$. To disentangle the CSI components induced by different spin polarizations ($R_{CSI}^{S_x}$, $R_{CSI}^{S_y}$, and $R_{CSI}^{S_z}$), we measure R_{NL} by sweeping an external magnetic field along the x - (H_x) and z -axes (H_z), inducing Hanle precession of the spin current [20] (See Methods for details). The spin transport properties of the pristine Gr and Gr/1T-TaS₂ heterostructure have been characterized individually in the same device using a non-local spin valve measurement (see Supplementary Note 5 for details) [38]. An electrical gate voltage (V_G) was applied to Gr to tune its Fermi level.

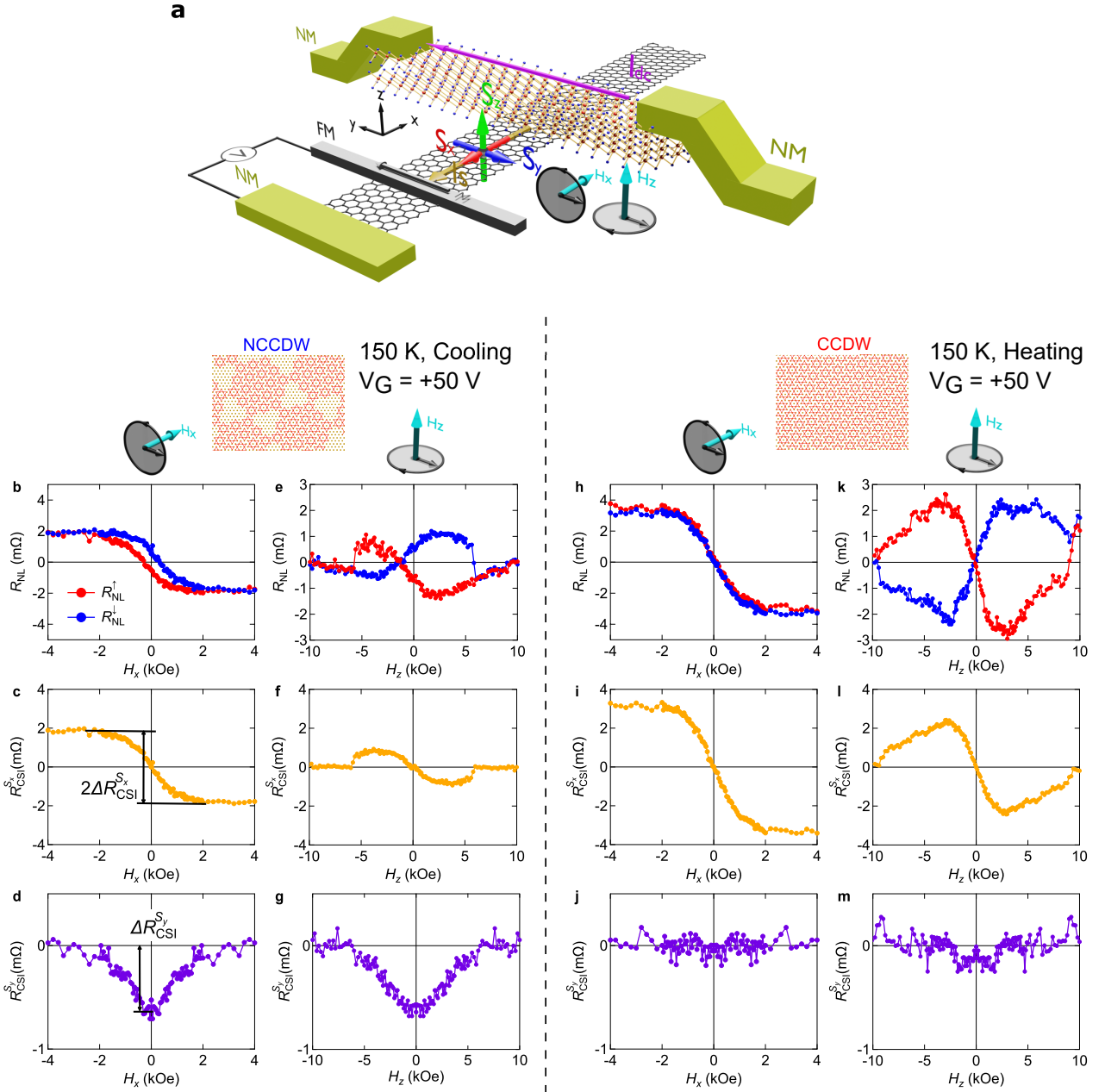


Figure 2. CSI characterization of Gr/1T-TaS₂ heterostructure Device 1 with different 1T-TaS₂ CDW phases. **a**, Schematic illustration of the CSI device. The device consists of a Gr/1T-TaS₂ heterostructure Hall bar cross junction, ferromagnetic (FM) nanowire electrodes (grey), and non-magnetic (NM) electrodes (light green). The bottom-right sketches illustrate the Hanle precession of the spin current under magnetic fields

applied along the x (H_x) and z (H_z) axes. **b**, Non-local CSI resistance (R_{NL}) measured as a function of H_x with the NCCDW phase of 1T-TaS₂. The initial magnetization directions of the FM electrode are set along the $+y$ (R_{NL}^\uparrow , red line) and $-y$ directions (R_{NL}^\downarrow , blue line). **c**, H_x -dependent CSI component induced by spin current with spin polarization along the x -axis ($R_{CSI}^{S_x}$) extracted by averaging the two curves in **b**. The amplitude of $R_{CSI}^{S_x}$ is labeled as $\Delta R_{CSI}^{S_x}$. **d**, H_x -dependent CSI component induced by spin current with spin polarization along the y -axis ($R_{CSI}^{S_y}$) obtained by symmetrizing the half of the difference of the two curves in **b**. The amplitude of $R_{CSI}^{S_y}$ is labeled as $\Delta R_{CSI}^{S_y}$. **e**, R_{NL}^\uparrow (red line) and R_{NL}^\downarrow (blue line) measured as a function of H_z with the NCCDW phase of 1T-TaS₂. The sudden jump of the two curves at $|H_z| \sim 5$ kOe is attributed to a magnetization switching of the FM electrode, but does not affect the spin precession feature of the curves. **f**, H_z -dependent $R_{CSI}^{S_x}$ obtained by antisymmetrizing the half of the difference of the two curves in **e**. **g**, H_z -dependent $R_{CSI}^{S_y}$ extracted by symmetrizing the half of the difference of the two curves in **e**. **h**, R_{NL}^\uparrow (red line) and R_{NL}^\downarrow (blue line) measured as a function of H_x with the CCDW phase of 1T-TaS₂. **i**, H_x -dependent $R_{CSI}^{S_x}$ acquired by averaging the two curves in **h**. **j**, H_x -dependent $R_{CSI}^{S_y}$ obtained by symmetrizing the half of the difference of the two curves in **h**. **k**, R_{NL}^\uparrow (red line) and R_{NL}^\downarrow (blue line) measured as a function of H_z with the CCDW phase of 1T-TaS₂. **l**, H_z -dependent $R_{CSI}^{S_x}$ acquired by antisymmetrizing the half of the difference of the two curves in **k**. **m**, H_z -dependent $R_{CSI}^{S_y}$ obtained by symmetrizing the half of the difference of the two curves in **k**. A constant baseline of 1.9, 2.9, 6.8, and 8.6 m Ω has been subtracted from the curves in **b**, **e**, **h**, and **k**, respectively. All data was collected at 150 K with a gate voltage $V_G = +50$ V.

2.2 CDW phase dependence of CSI

Figure 2 illustrates the dependence of the CDW phase on the CSI characterization in Device 1 (bilayer Gr/60-nm-thick 1T-TaS₂) at $V_G = +50$ V. All the measurements were performed at 150 K, where either the NCCDW or the CCDW phase of 1T-TaS₂ can be stabilized by cooling or heating (Fig. 1b), while the Gr properties remain constant. Figure 2b displays the H_x -dependent R_{NL} at the NCCDW phase. The red (R_{NL}^\uparrow) and blue (R_{NL}^\downarrow) curves were measured with the magnetization \mathbf{M} of the FM electrode (Fig. 2a) initially set along the $+y$ and $-y$ directions. To extract the different CSI components, we define $R_{NL}^{\text{avg}}(H_x) = (R_{NL}^\uparrow + R_{NL}^\downarrow)/2$ and $R_{NL}^{\text{diff}}(H_x) = (R_{NL}^\uparrow - R_{NL}^\downarrow)/2$. This average corresponds to the CSI component of the spins polarized along the x -axis ($R_{CSI}^{S_x}(H_x) \equiv R_{NL}^{\text{avg}}(H_x)$) and the difference includes both the CSI components of the spins polarized along the y - ($R_{CSI}^{S_y}$) and z -axes ($R_{CSI}^{S_z}$). $R_{CSI}^{S_y}$ and $R_{CSI}^{S_z}$ can be further distinguished by symmetrizing and antisymmetrizing $R_{NL}^{\text{diff}}(H_x)$, respectively (see Methods for details).

The extracted $R_{CSI}^{S_x}$ is presented as a function of H_x in Fig. 2c, revealing an S-like line shape. The value of $R_{CSI}^{S_x}$ increases with increasing $|H_x|$ and reaches a maximum of 1.9 m Ω at $|H_x| \sim 2$ kOe, where \mathbf{M} is fully saturated along the x -axis. Figure 2d illustrates the H_x -dependence of $R_{CSI}^{S_y}$, which has a maximum of 0.7 m Ω when H_x is zero and decreases as H_x increases until it vanishes at $|H_x| \sim 2$ kOe. This CSI component is confirmed by measuring R_{NL} as a function of H_y , which shows a squared hysteresis loop (See Supplementary Note 7 for details). $R_{CSI}^{S_z}$ is not shown, as it is below the noise level. Note that the

S -like line shape of $R_{\text{CSI}}^{S_x}$ with H_x could also be a spurious effect originating from the ordinary Hall effect in Gr induced by the stray field of the FM electrode [39]. To confirm the spin transport origin of the signal, i.e., CSI, R_{NL} was measured by sweeping H_z to obtain the spin precession in the x - y plane. Figure 2e displays R_{NL}^\uparrow and R_{NL}^\downarrow as a function of H_z . In this case, $R_{\text{CSI}}^{S_x}$ and $R_{\text{CSI}}^{S_y}$ are extracted by defining $R_{\text{NL}}^{\text{diff}}(H_z) = (R_{\text{NL}}^\uparrow - R_{\text{NL}}^\downarrow)/2$ and taking the antisymmetric and symmetric part, respectively (see Methods). Figure 2f shows that $R_{\text{CSI}}^{S_x}$ exhibits a clear antisymmetric Hanle precession feature vs. H_z , reaching a maximum of 0.9 m Ω at $H_z \sim 3$ kOe. $R_{\text{CSI}}^{S_y}$ is plotted as a function of H_z in Fig. 2g, showing a maximum of 0.7 m Ω when H_z is zero and decreasing with increasing H_z . The maxima of $R_{\text{CSI}}^{S_y}$ in both H_x - and H_z -dependent measurements are in good agreement. These results provide unequivocal proof that the CSI signals in Figs. 2b and 2e are induced by the CSI components of spin currents polarized along the x - and y -axes. We determine the amplitude of $R_{\text{CSI}}^{S_x}$ and $R_{\text{CSI}}^{S_y}$ using, respectively, the step height in Fig. 2c ($\Delta R_{\text{CSI}}^{S_x} \equiv (R_{\text{CSI}}^{S_x}(H_x = 2 \text{ kOe}) - R_{\text{CSI}}^{S_x}(H_x = -2 \text{ kOe}))/2$) and the maximum value in Fig. 2d ($\Delta R_{\text{CSI}}^{S_y} \equiv |R_{\text{CSI}}^{S_y}(H_x = 0)|$).

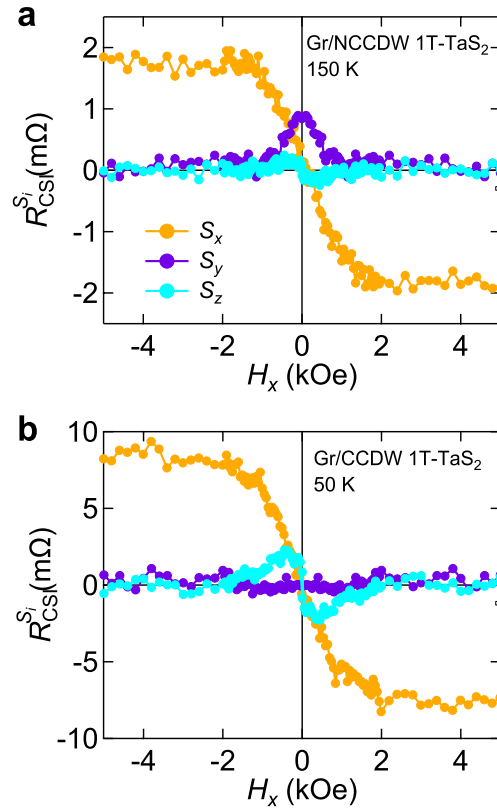


Figure 3. Spin-polarization direction dependent CSI in Device 2. Different components of the CSI ($R_{\text{CSI}}^{S_i}$) extracted from the non-local CSI resistance measured as a function of H_x in Device 2. $R_{\text{CSI}}^{S_i}$ in Gr/NCCDW 1T-TaS₂ heterostructure at 150 K and in Gr/CCDW 1T-TaS₂ heterostructure at 50 K are displayed in **a** and **b**, respectively. $R_{\text{CSI}}^{S_i}$ originating from spin currents with spin polarization along the x ($R_{\text{CSI}}^{S_x}$), y ($R_{\text{CSI}}^{S_y}$), and z ($R_{\text{CSI}}^{S_z}$)

axes are plotted as orange, purple, and cyan curves, respectively. All the measurements were performed without applying a gate voltage. See Supplementary Note 6 for the raw data.

Similar measurements were conducted after driving the NCCDW-CCDW phase transition in 1T-TaS₂ and stabilizing the CCDW phase at 150 K. The resulting R_{NL} and the corresponding $R_{\text{CSI}}^{S_x}$ and $R_{\text{CSI}}^{S_y}$ are plotted as a function of H_x (Figs. 2h-2j) and H_z (Figs. 2k-2m). The *S*-like (antisymmetric Hanle precession) line shape of $R_{\text{CSI}}^{S_x}$ as a function of H_x (H_z) indicates that the CSI component induced by *x*-polarized spin current persists in the CCDW phase. $\Delta R_{\text{CSI}}^{S_x}$ increases by approximately a factor of two after the phase transition. Interestingly, regardless of whether the magnetic field is applied along the *x*- or *z*-axis, $R_{\text{CSI}}^{S_y}$ is nearly zero. This result evidences that the unconventional CSI is switched off in our heterostructure when 1T-TaS₂ is in the CCDW phase.

To investigate whether the disappearance of the unconventional CSI in Gr/1T-TaS₂ heterostructure during the phase transition is reproducible, we repeated the experiment in another device (Device 2, monolayer Gr/100-nm-thick 1T-TaS₂). $R_{\text{CSI}}^{S_x}$, $R_{\text{CSI}}^{S_y}$, and $R_{\text{CSI}}^{S_z}$ obtained with the NCCDW and CCDW phases are plotted as a function of H_x in Figs. 3a and 3b, respectively. We find that $R_{\text{CSI}}^{S_y}$ disappears again after the phase transition while $R_{\text{CSI}}^{S_x}$ exists regardless of the CDW phase, confirming the previous observation.

Interestingly, although $R_{\text{CSI}}^{S_z}$ in Device 1 is lower than the noise level, we clearly observe $R_{\text{CSI}}^{S_z}$ in Device 2 when 1T-TaS₂ is in either the NCCDW or the CCDW phase, as shown by the clear antisymmetric Hanle precession cyan curves in Figs. 3a and 3b, respectively. This CSI component is also detected in another device (Device 3, few-layer Gr/22-nm-thick 1T-TaS₂), indicating that the number of Gr layers is not the reason for observing $R_{\text{CSI}}^{S_z}$. We note that the spin injection efficiency of the ferromagnet, estimated from non-local spin valve measurements, is much lower in Device 1 than in Devices 2 and 3 (See Supplementary Note 5). Compared to the relatively large $\Delta R_{\text{CSI}}^{S_x}$ and $\Delta R_{\text{CSI}}^{S_y}$, especially when 1T-TaS₂ is in the NCCDW phase (Fig. 3a), the lower spin injection efficiency in Device 1 prevents the detection of the small $R_{\text{CSI}}^{S_z}$ component.

We also investigated CSI in Device 3 when 1T-TaS₂ is in the ICCDW phase (See Supplementary Note 8 for details). All three CSI components are observed at 360 K. As discussed above, the transport in 1T-TaS₂ is principally governed by the normal state, both in the NCCDW and ICCDW phases. Conversely, in the CCDW phase, the CDW state predominates, thereby instigating insulating-like behavior. These results suggest that the phase-dependent switching of the unconventional CSI ($R_{\text{CSI}}^{S_y}$) is linked to the change in the transport regime (that is, commensurability) of 1T-TaS₂.

2.3 Temperature and gate voltage dependencies of CSI

After confirming an omnidirectional CSI and a phase-transition-driven switchable unconventional CSI, we studied the temperature (T) and gate voltage (V_G) dependencies of CSI. $\Delta R_{\text{CSI}}^{S_x}$ and $\Delta R_{\text{CSI}}^{S_y}$ extracted

from Device 1 are plotted as a function of T in Fig. 4a. We observe that both $\Delta R_{\text{CSI}}^{S_x}$ and $\Delta R_{\text{CSI}}^{S_y}$ increase as T decreases, regardless of the phase of 1T-TaS₂. Furthermore, $\Delta R_{\text{CSI}}^{S_x}$ exhibits a phase-related hysteresis loop with T , which is consistent with the resistance hysteresis loop of 1T-TaS₂ (Fig. 1b). This agreement indicates that the resistance of 1T-TaS₂ influences the CSI output in Gr/1T-TaS₂ heterostructures.

Figure 4b illustrates $\Delta R_{\text{CSI}}^{S_x}$ and $\Delta R_{\text{CSI}}^{S_y}$ extracted from Device 1 at 150 K as a function of V_G . All the CSI components follow a similar trend with respect to V_G : their magnitudes reach a minimum when $V_G = -40$ V, i.e., the charge neutrality point of the Gr/1T-TaS₂ heterostructure (Fig. 4c), and increase as V_G increases from -40 V. The values reach saturation after V_G is increased up to $+40$ V. This behavior differs from that observed in the resistance of Gr/1T-TaS₂ heterostructure (Fig. 4c). To understand the observed V_G dependence, we measured the charge and spin transport properties of Device 1 at 150 K with different V_G . The resistance of 1T-TaS₂ exhibits negligible changes with V_G (Fig. S4b and S4c in Supplementary Note 4). In contrast, the spin injection efficiency, given by the non-local spin valve signal shown in Fig. 4d (see details on the measurement in Supplementary Note 5), shows a similar dependence on V_G as the CSI output. Therefore, we suggest that the tuning of the CSI output by the gate voltage can be primarily attributed to the gate tuning of the spin injection efficiency at the Gr/FM electrode interface. Similar T and V_G dependencies of CSI are obtained in Device 3 (see Supplementary Note 8).

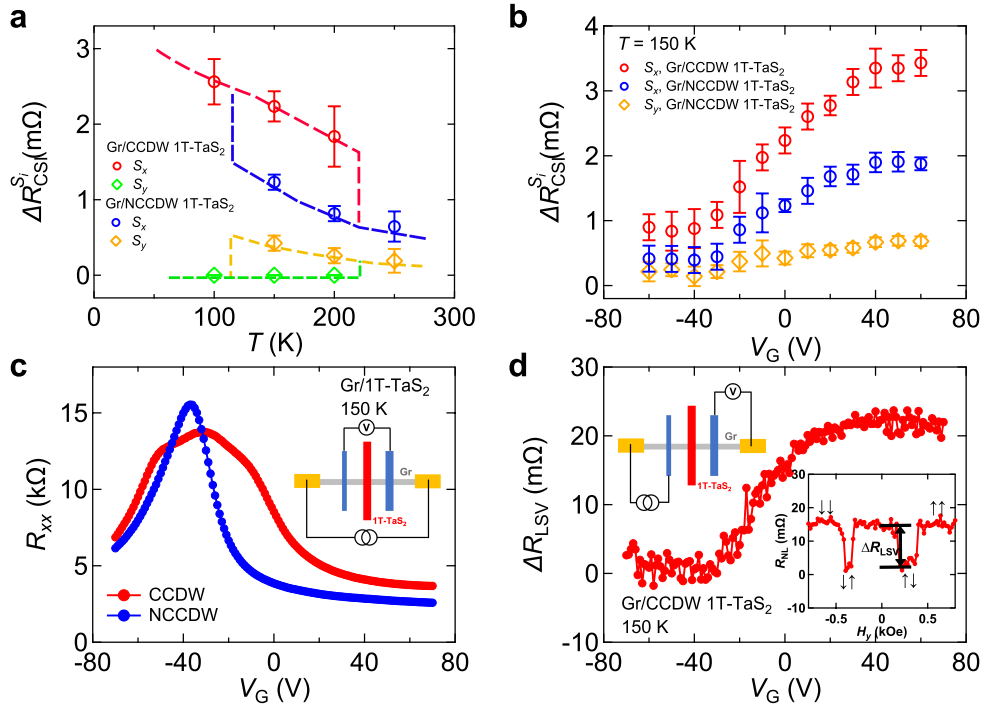


Figure 4. Temperature and gate voltage dependencies of CSI in Device 1. a, Temperature (T) dependence of $\Delta R_{\text{CSI}}^{S_i}$ measured without adding gate voltage. $\Delta R_{\text{CSI}}^{S_x}$ in the heterostructure in the NCCDW (CCDW) phase of 1T-TaS₂ are displayed by red (blue) circles. $\Delta R_{\text{CSI}}^{S_y}$ in the heterostructure in the NCCDW phase of 1T-TaS₂ is shown by orange diamonds. The vanished $\Delta R_{\text{CSI}}^{S_y}$ in the heterostructure in the CCDW phase of 1T-TaS₂ is represented by the green diamonds, with all the values equal to zero. The dashed curves are a guide to the eye

for the hysteresis loops observed in ΔR_{CSI}^{Si} . **b**, V_G dependence of ΔR_{CSI}^{Si} measured at $T = 150$ K. **c**, V_G dependence of the longitudinal resistance of the Gr/1T-TaS₂ heterostructure (R_{xx}) when 1T-TaS₂ is at the CCDW (red circles) and NCCDW (blue circles) phases. Inset: Sketch of the measurement configuration. **d**, V_G dependence of the non-local spin valve signal (ΔR_{LSV}) measured across the Gr/CCDW 1T-TaS₂ heterostructure at 150 K. Insets: Sketch of the measurement configuration (left) and the non-local resistance of the spin valve (R_{NL}) measured with $V_G = 0$ V (right). The definition of ΔR_{LSV} is labelled. Error bars are calculated using the standard deviation associated with the statistical average of R_{CSI}^{Si} in both the positive and negative magnetic field ranges.

2.4 The origin of the CSI

The observed CSI in the Gr/1T-TaS₂ heterostructure can have different origins: the SHE inherent to the bulk 1T-TaS₂, the interfacial SHE arising from the spin-orbit proximity, and the REE generated by the broken inversion symmetry at the interface. To gain insight into the underlying mechanisms of tunable CSI driven by the commensurability of the CDW phase, we perform first-principles calculations based on density functional theory (see Methods) to analyze the CSI of bulk 1T-TaS₂ and of the Gr/1T-TaS₂ van der Waals heterostructure in the normal and the CCDW states of 1T-TaS₂.

We investigate first the SHE of bulk 1T-TaS₂ by calculating the spin Hall conductivity tensor σ_{ij}^k , where i, j , and k represent the directions of j_s, j_c , and S , respectively. In our measurement, the charge current is along the y -axis, whereas the spin current direction in the bulk 1T-TaS₂ can be either along the x -axis ($j_{s,x}$) or along the z -axis ($j_{s,z}$) due to the absorption from Gr, as seen in metallic systems [38]. Table 1 summarizes the calculated σ_{ij}^k values of possible elements in our measurement configuration, determined by the spin Berry curvature component Ω_{ij}^k (see Supplementary Note 9 for details). On the one hand, for $j_{s,x}$, σ_{xy}^z is much larger than σ_{xy}^x and σ_{xy}^y in the normal state. These values suggest the R_{CSI}^{Sz} would be the largest CSI component detected in the NCCDW or ICCDW phases of 1T-TaS₂. However, this prediction contradicts our experimental results, leading us to exclude the possibility of CSI originating from the SHE of bulk 1T-TaS₂ induced by $j_{s,x}$. On the other hand, for $j_{s,z}$, σ_{zy}^y and σ_{zy}^z are strictly zero (due to symmetry constrain [40]) or negligible for the normal and CCDW states, respectively, indicating that the conventional SHE (σ_{zy}^x) in bulk 1T-TaS₂ is the only bulk 1T-TaS₂-originated component that can contribute to the observed R_{CSI}^{Sx} .

Table 1. Spin Hall conductivity in bulk 1T-TaS₂ and the graphene/1T-TaS₂ heterostructure calculated in the CCDW and normal phases of 1T-TaS₂. The spin Hall conductivity is represented by σ_{ij}^k , where i, j , and k represent the spin current, charge current, and spin polarization directions respectively. Since σ_{ij}^k is very sensitive to the crystallographic orientation, each number indicates the maximum values of σ_{ij}^k for any possible crystal orientations. All units are in $((\hbar/e) S/cm)$.

		σ_{xy}^x	σ_{xy}^y	σ_{xy}^z	σ_{zy}^x	σ_{zy}^y	σ_{zy}^z
1T-TaS ₂	normal	6.5	6.5	59.6	22.0	-	-
	CDW	9.0	8.0	24.0	15.0	3.0	1.0
Gr/1T-TaS ₂	normal	6.0	6.0	53.0	-	-	-
	CDW	15.0	20.0	18.0	-	-	-

Next, we investigate the interfacial SHE of the Gr/1T-TaS₂ heterostructure. The calculated σ_{ij}^k values are summarized in Table 1 (see Supplementary Note 9 for details). By nature of the interfacial effect, the direction of the spin current is constrained to the x -axis. In the calculated spin Berry curvature, it becomes evident that the Dirac band of Gr mostly contributes to the integration when the 1T-TaS₂ is in the CCDW phase. Conversely, the contribution from 1T-TaS₂ bands predominates in the Gr/normal state 1T-TaS₂ heterostructure (See Supplementary Note 9 for details). Such feature implies that the source of the interfacial SHE shifts from the 1T-TaS₂ side to the Gr side following the transition from the NCCDW to the CCDW phase. In the normal state, the conventional component σ_{xy}^z shows a much larger value compared to the unconventional components σ_{xy}^x and σ_{xy}^y . However, its contribution to the CSI output should be limited because most of the current flows in the bulk 1T-TaS₂. In the CCDW state, σ_{xy}^z is smaller than that in the normal state. In this case, the current redistributes and passes predominantly through the Gr side due to the enhanced resistance of CCDW 1T-TaS₂, indicating that the CSI output should increase. These properties are consistent with $\Delta R_{\text{CSI}}^{S_z}$ observed in Device 2 (Fig. 3), suggesting that the CSI induced by S_z -spin current is due to the conventional interfacial SHE. Note that unconventional σ_{xy}^x and σ_{xy}^y are comparable to σ_{xy}^z in the CCDW state, indicating that they can contribute to $R_{\text{CSI}}^{S_x}$ and $R_{\text{CSI}}^{S_y}$, respectively. However, the finite σ_{xy}^y is inconsistent with the vanishing $R_{\text{CSI}}^{S_y}$ in our experiment.

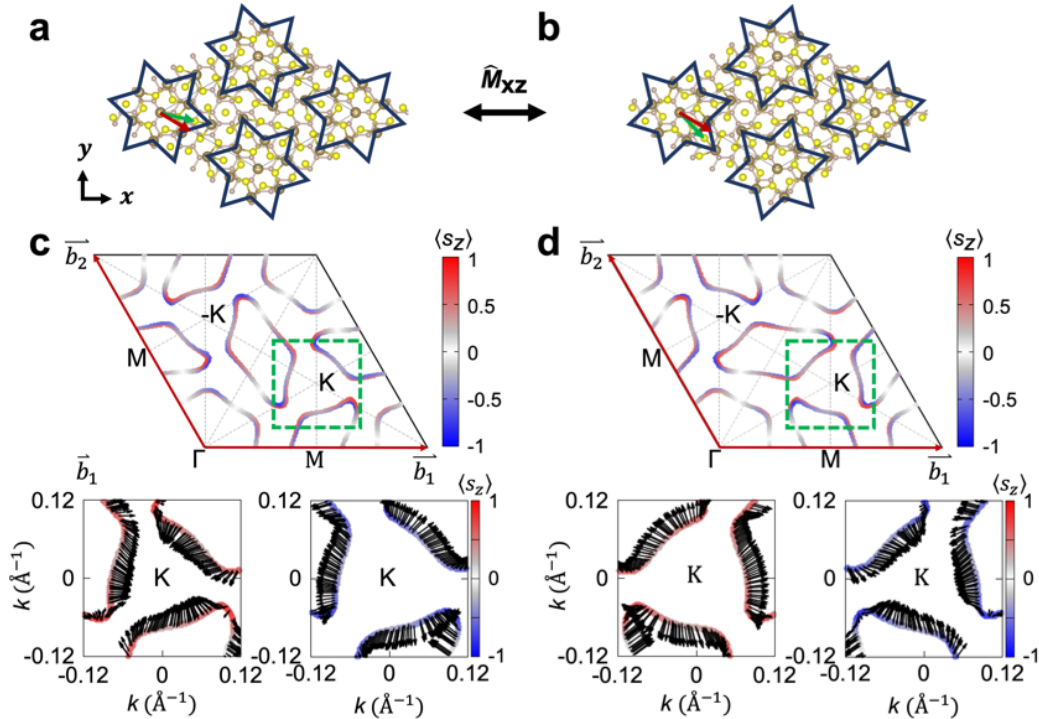


Figure 5. First-principles calculations for Rashba spin texture in Gr/1T-TaS₂ heterostructures. **a, b**, Two possible chiral states of Gr/CCDW 1T-TaS₂ heterostructures with opposite handedness. The green and red arrows indicate unit vector of normal and CCDW 1T-TaS₂, respectively, which have either +13.9° or -13.9° rotation angle. They are mirror symmetric corresponding to the \hat{M}_{xz} mirror operator. **c, d**, Handedness-dependent spin-resolved Fermi surfaces and Rashba spin textures of proximitized Dirac bands. Near the K point

(highlighted by a green box), red and blue colors show spin splitting in the Dirac bands due to the Rashba spin-orbit coupling. The lower two panels show in-plane spin textures of inner (left) and outer (right) Rashba bands. Only the radial spin components are opposite in the chiral structures with opposite handedness.

Finally, we consider the REE as the source of our observed CSI. On the one hand, the conventional REE can contribute to $R_{\text{CSI}}^{S_x}$ in our setup. On the other hand, recent studies have revealed that $R_{\text{CSI}}^{S_y}$ in Gr/TMDC van der Waals heterostructures with a twist angle [26] [27] is related to an unconventional REE (UREE) induced by radial spin textures in the Rashba bands due to the lack of a mirror plane [29] [30] [31] [32]. Indeed, we observed a radial spin texture in both Gr/CCDW 1T-TaS₂ and Gr/normal 1T-TaS₂ heterostructures (Fig. 5 and Fig. S17 in Supplementary Note 9) in our calculations. Since UREE can contribute to $R_{\text{CSI}}^{S_y}$, it is reasonable to expect a non-zero $R_{\text{CSI}}^{S_y}$ in both normal and CCDW 1T-TaS₂ states. This result, as in the case of the finite interfacial σ_{xy}^y , also contradicts our experimental observation.

To reconcile the theory with experimental observations, we examine the role of chirality in the Gr/CCDW 1T-TaS₂ heterostructures, as described in Figs. 5a and 5b. It is well known that the lattice vectors of CCDW 1T-TaS₂ are rotated by either +13.9° or -13.9° from normal 1T-TaS₂, resulting in two helical states with opposite handedness [41]. These helical states are mirror-symmetric with respect to any mirror plane perpendicular to the TaS₂ layer and can be simultaneously observed in a single 1T-TaS₂ flake [41]. Note that this helical domain is intrinsic and is only described by mirroring, not by rotation, and is distinct from a trivial polycrystalline domain. In the presence of Gr/CCDW 1T-TaS₂ interface, the inversion symmetry is broken. This leads to the transformation of the helicity of 1T-TaS₂ into the chirality of the resulting heterostructures. In general, arbitrary twist angles between Gr and 1T-TaS₂ may break the mirror relation between two chiral heterostructures. However, to better grasp the underlying physics, we focused on simple examples that exhibit the mirror relation between two chiral heterostructures, (\widehat{M}_{xz} , in our case) and investigated the role of chiral domains.

We present the spin-resolved Fermi surfaces of both chiral heterostructures in Figs. 5c and 5d. Near the K point (indicated by a green box), we observed a Gr Dirac band with distinct spin splitting, resulting in inner (red) and outer (blue) Rashba bands. The in-plane spin textures of both Rashba bands are shown in the lower two panels. Our results reveal opposite radial spin textures for different handedness, while the conventional Rashba component remains the same in both chiral states, which means that the radial spin is locked to the chirality [42] [43][42][43]. This is because the \widehat{M}_{xz} operation flips S_x , S_z , and k_y , but not S_y and k_x . Here k_x (k_y) represents the momentum along the x (y)-axis. These results imply that conventional REE is preserved whereas UREE should disappear when both chiral CDW structures coexist. The effect of chiral domain on the interfacial SHE can also be deduced from the quantity $S_{ij}^k = v_i S_k v_j$, where v represents the velocity of electrons [40]. This quantity has the same symmetry as Ω_{ij}^k . Similar to UREE, $\widehat{M}_{xz} \Omega_{xy}^y = v_x S_y (-v_y) = -\Omega_{xy}^y$, indicating that the total interfacial σ_{xy}^y is also canceled out if the two handedness coexist.

Note that the CDW domains in the NCCDW phase of 1T-TaS₂ exhibit an average size of ~ 10 nm at 200 K [44] [45]. The chiral domain expands and merges during the NCCDW-CCDW phase transition, which can increase its size in the CCDW phase. However, this scale is much smaller than our micrometer-level devices. Although millimeter-size chiral domains have been reported in recent studies [36, 46], the size could also be restricted by the appearance of impurities [41]. Therefore, we deduce that the contributions from UREE and interfacial σ_{xy}^y are canceled out due to the mixed chiral domains with opposite handedness, i.e., the vanishing $R_{\text{CSI}}^{S_y}$ in our experiments, whereas the conventional REE and interfacial σ_{xy}^x contribute to the observed $R_{\text{CSI}}^{S_x}$. Hence, it can be concluded that the intrinsic chirality of the CCDW phase governs the evolution of both UREE and the interfacial unconventional SHE. Alternative hypothesis, for instance a non-uniform current distribution along the x -axis arising from the high-conductivity normal-phase channels in between the commensurate star-of-David domains of the NCCDW phase, could potentially generate the $R_{\text{CSI}}^{S_y}$ component by the conventional SHE. However, we maintain a net zero current along the x -axis during the measurements, ruling out this scenario as the origin of the unconventional CSI.

Our observation provides new opportunities for designing functional spintronic devices with a degree of freedom from the material itself. For instance, the tunable CSI could be exploited in spin-orbit torque memory devices, where only specific unconventional CSI components contribute to the deterministic switching of perpendicular magnetization. This process has been demonstrated in low-symmetry materials [49] [50] [51] [52], where the underlying symmetry of CSI phenomena, and the allowed charge-spin response tensor, is governed by the crystal symmetry [40] [53]. The present 1T-TaS₂, with tunable CDW between high and low symmetry crystalline phases, simplifies such geometric obstacle and offers an enticing platform for realizing such on-demand switchable CSI.

3. Conclusion

In summary, we report the first demonstration of tunable CSI in Gr/1T-TaS₂ van der Waals heterostructures exploiting the phase transition of the CDW in the TMDC. We observe omnidirectional CSI (i.e., with spins oriented in all three directions) in the heterostructures when the CDW in 1T-TaS₂ does not show commensurability. Whereas the CSI components induced by S_x - and S_z -polarized spin currents are enhanced after a phase transition to a commensurate state, the one induced by S_y -polarized spin currents is switched off. By comparing our experimental results with first-principles calculations, we conclude that the disappearance of this CSI component is due to the appearance of chiral CDW multidomains. Our findings provide insights into the interplay between proximity, commensurability and chirality of the CDW in the Gr/1T-TaS₂ system and establish it as a platform for low-dimensional functional spin-orbitronic devices.

4. Experimental Section

Device fabrication

The graphene/1T-TaS₂ heterostructures were assembled by the dry viscoelastic transfer technique. Elongated graphene flakes were first exfoliated from highly oriented pyrolytic graphite (HQ Graphene) and deposited on highly *n*-type doped Si substrates with a 300-nm-thick SiO₂ layer. The monolayer and bilayer graphene flakes were distinguished based on the contrast using an optical microscope and confirmed by Raman spectroscopy. The 1T-TaS₂ flakes were exfoliated from a single crystal provided by 2D Semiconductors (Device 1) and by HQ Graphene (Devices 2 and 3) onto a piece of polydimethylsiloxane (PDMS). After identifying strips with suitable width and thickness (confirmed later by an atomic force microscopy) using an optical microscope, the 1T-TaS₂ flakes were then transferred from the PDMS stamp to the SiO₂/Si substrate, where they formed Hall bar cross junctions with the elongated graphene flakes. The exfoliation of 1T-TaS₂ flakes and transfer processes were carried out in a glovebox with an Ar atmosphere. Non-magnetic Pd (5 nm)/Au (45 nm) electrodes were used to contact the graphene and 1T-TaS₂ and fabricated using the standard processes of e-beam lithography, evaporation, and lift-off. TiO_x/Co/Au ferromagnetic (FM) electrodes were deposited on the graphene flake to inject/detect the spin current and fabricated using the same processes as Pd/Au electrodes. During the evaporation process, ~0.3 nm of Ti was first deposited, followed by a 10-min ambient oxidization process that formed the TiO_x layer. Then, 35 nm of Co and 15 nm of Au were evaporated. The 15-nm-thick Au layer was a capping layer to protect the Co layer from oxidization. The width of FM electrodes was either 150 or 350 nm to give different shape anisotropies.

Electrical measurements

Local and non-local magnetotransport measurements were performed in a physical property measurement system (PPMS) by Quantum Design, where temperature was varied and magnetic fields were applied in different directions. The measurements were carried out using a dc reversal technique with a Keithley 2182 nanovoltmeter and a 6221 current source. A back-gate voltage was applied to the highly *n*-type doped Si substrate using a Keithley 2636B source meter unit to adjust the Fermi level of the graphene.

Separation of the different CSI components

In our CSI measurements, the spin polarization (S) of the spin current (j_s) diffusing in graphene is controllable by a magnetic field. By applying an external magnetic field along the x -axis (H_x) or z -axis (H_z), which respectively correspond to the in-plane and out-of-plane hard axes of the FM electrode, the spin in the spin current undergoes precession in the y - z or x - y plane. These precessions give additional spin-polarization components in the spin current. The magnetization \mathbf{M} of the FM electrode is also pulled by the external magnetic field. The amplitude of different CSI components ($\Delta R_{\text{CSI}}^{S_i}$) is thus proportional to the projection of \mathbf{M} along the corresponding spin polarization direction (S_i) of the spin current. To distinguish the components induced by a spin current with different polarizations, the non-local CSI resistance R_{NL} is measured as a function of H_x or H_z .

By scanning H_x , the R_{NL} component induced by S_x ($R_{\text{CSI}}^{S_x}$) is zero when $H_x = 0$ because the initial \mathbf{M} is perpendicular to S_x . The value of $R_{\text{CSI}}^{S_x}$ increases as H_x increases and finally saturates when \mathbf{M} is fully

aligned along the x -axis. This yields an S -like line shape similar to the conventional SHE in metals [38] or the REE in 2D systems [21]. $R_{\text{CSI}}^{S_x}$ is unaffected by the initial direction of \mathbf{M} ($+y$ or $-y$) as its value is only determined by the projection of \mathbf{M} along the x -axis. On the other hand, because the spin current precesses within the y - z plane under a small H_x , the R_{NL} components originating from S_y ($R_{\text{CSI}}^{S_y}$) and S_z ($R_{\text{CSI}}^{S_z}$) show a spin precession feature as a function of H_x . Considering the initial \mathbf{M} along the y -axis, the precession of $R_{\text{CSI}}^{S_y}$ and $R_{\text{CSI}}^{S_z}$ should show symmetric and antisymmetric line shapes, respectively, as reported in other Gr/TMDC heterostructures [20] [21] [22] [24] [26] [27]. The signs of $R_{\text{CSI}}^{S_y}$ and $R_{\text{CSI}}^{S_z}$ reverse after switching the initial direction of \mathbf{M} because the initial projections of \mathbf{M} onto the y -axis are opposite. Both $R_{\text{CSI}}^{S_y}$ and $R_{\text{CSI}}^{S_z}$ will decrease to zero at high H_x due to the x -axis pulling of \mathbf{M} and the spin dephasing. Based on these properties, we can separate $R_{\text{CSI}}^{S_x}$, $R_{\text{CSI}}^{S_y}$, and $R_{\text{CSI}}^{S_z}$ by measuring R_{NL} with the initial direction of \mathbf{M} set along the $+y$ (R_{NL}^\uparrow) and $-y$ (R_{NL}^\downarrow) directions. $R_{\text{CSI}}^{S_x}$ can be extracted by taking their average ($R_{\text{NL}}^{\text{avg}}(H_x) = (R_{\text{NL}}^\uparrow + R_{\text{NL}}^\downarrow)/2$), since the sign of $R_{\text{NL}}^{S_x}$ is the same in both cases. The contribution of $R_{\text{CSI}}^{S_x}$ can be removed by taking half of the difference ($R_{\text{NL}}^{\text{diff}}(H_x) = (R_{\text{NL}}^\uparrow - R_{\text{NL}}^\downarrow)/2$), where the $R_{\text{CSI}}^{S_y}$ and $R_{\text{CSI}}^{S_z}$ contributions remain because their signs are opposite after reversing the initial direction of \mathbf{M} . $R_{\text{CSI}}^{S_y}$ and $R_{\text{CSI}}^{S_z}$ can be further separated by symmetrizing and antisymmetrizing $R_{\text{NL}}^{\text{diff}}(H_x)$, respectively, due to their different precession features.

The line shapes of R_{NL} measured under H_z are similar. In this case, the spin current precesses in the x - y plane under a small H_z . $R_{\text{CSI}}^{S_y}$ and $R_{\text{CSI}}^{S_x}$ are symmetric and antisymmetric against H_z . Their signs reverse after switching the initial direction of \mathbf{M} . Therefore, $R_{\text{CSI}}^{S_y}$ and $R_{\text{CSI}}^{S_x}$ can be separated by symmetrizing and antisymmetrizing $R_{\text{NL}}^{\text{diff}}(H_z)$ when H_z is scanned. Although $R_{\text{CSI}}^{S_z}$ vs. H_z should have an S -like line shape, similar to $R_{\text{CSI}}^{S_x}$ measured vs. H_x , a linear background exists in R_{NL} because of the large ordinary Hall effect in Gr. Hence, it is difficult to determine $R_{\text{CSI}}^{S_z}$ using an H_z -dependent measurement.

First-principles calculations

We performed first-principles calculations based on density functional theory (DFT) [54] as implemented in Quantum Espresso package (QE) [55] [56]. The exchange-correlation functional was treated within the generalized gradient approximation of Perdew-Burke-Ernzerhof (PBE) [57]. The kinetic energy cutoff of electronic wavefunctions and charge density were chosen to be 80 and 640 Ry, respectively. To mimic the 2D layered structure, we included a large vacuum region in periodic cells, and used Grimme-D3 van der Waals correction [58] where necessary. The spin-orbit coupling was included in the electronic structure calculations. The k -grid meshes were chosen to be $15 \times 15 \times 9$, $5 \times 5 \times 9$, and $4 \times 4 \times 1$ for bulk normal 1T-TaS₂, bulk CCDW 1T-TaS₂, and graphene/1T-TaS₂ heterostructures, respectively.

The intrinsic spin Hall conductivity $\sigma_{\alpha\beta}^y$ was calculated by the Kubo-Greenwood formula as [59]

$$\sigma_{\alpha\beta}^{\gamma}(\varepsilon) = \frac{\hbar}{\Omega_C N_k} \sum_{\mathbf{k}} \sum_n f_{n\mathbf{k}} \sum_{m \neq n} \frac{2\text{Im}[\langle n\mathbf{k} | \hat{j}_{\alpha}^{\gamma} | m\mathbf{k} \rangle \langle m\mathbf{k} | -e\hat{v}_{\beta} | n\mathbf{k} \rangle]}{(\varepsilon_{n\mathbf{k}} - \varepsilon_{m\mathbf{k}})^2 + \eta^2},$$

where Ω_C and N_k indicate the cell volume and the number of k-points used for k-space sampling, $f_{n\mathbf{k}}$ indicates Fermi-Dirac distribution, $\hat{j}_{\alpha}^{\gamma}$ is the spin current operator defined as $\hat{j}_{\alpha}^{\gamma} = \frac{1}{2}\{\hat{s}^{\gamma}, \hat{v}_{\alpha}\}$ and \hat{s}^{γ} and $\hat{v}_{\alpha,\beta}$ are spin and velocity operators, respectively. η is an adjustable smearing parameter. The numerical calculations were performed by Wannier90 package [60] [61] [62] [63]. For wannierization, d , p , and p_z orbital projections were used for Ta, S, and C atoms, and additional sp^2 orbital projections were alternatively added to the C atoms. To obtain the converged results, we used a fine k-mesh grid of $300 \times 300 \times 180$ for normal 1T-TaS₂, $80 \times 80 \times 160$ for CCDW 1T-TaS₂, and $600 \times 600 \times 1$ for Gr/1T-TaS₂ heterostructures. The corresponding broadening constant of η was chosen to be 10 meV. In the Gr/1T-TaS₂ heterostructures, we used an effective thickness of 9.46 Å when we evaluate their $\sigma_{\alpha\beta}^{\gamma}$ in units of $((\hbar/e) S/cm)$ (presented in Table 1).

Acknowledgements

We thank F. de Juan and H. Ochoa for the fruitful discussions. We acknowledge funding by the “Valleytronics” Intel Science Technology Center, the Spanish MICINN (Project No. PID2021-122511OB-I00 and “Maria de Maeztu” Units of Excellent Programme No. CEX2020-001038-M), the European Union H2020 under the Marie Skłodowska-Curie Actions (Project Nos. 0766025-QuESTech and 955671-SPEAR), and Diputación de Gipuzkoa (Project No. 2021-CIEN-000037-01). S.L. and T.L. are partially supported by National Science Foundation through the University of Minnesota MRSEC under Award Number DMR-2011401. Z.C. and J.I.-A. acknowledge postdoctoral fellowship support from “Juan de la Cierva” Programme by the Spanish MICINN (grants No. FJC2021-047257-I and FJC2018-038688-I, respectively). S.L. is also partially supported by Basic Science Research Program through the National Research Foundation of Korea (NRF) funded by the Ministry of Education (NRF-2021R1A6A3A14038837). N.O. thanks the Spanish MICINN for support from a Ph.D. fellowship (Grant No. BES-2017-07963). B. M.-G. thanks support from “Ramón y Cajal” Programme by the Spanish MICINN/AEI (grant no. RYC2021-034836-I).

Author contributions

Z.C. and F.C. conceived this study. Z.C. fabricated and characterized the devices, performed the electrical measurements, and analyzed the data with the help of H.Y., E.D., C.K.S, J.I.-A., F.H., and N.O.. S.L. and T.L. performed the first-principles calculations. All authors contributed to the discussion on the results. Z.C., S.L., and F.C. wrote the manuscript with input from all authors.

Competing interests

The authors declare no competing interests.

References

- [1] K. Garello, F. Q. Yasin, S. Couet, L. Souriau, J. Swerts, S. Rao, S. Van Beek, W. Kim, Y. Liu, S. Kundu, D. Tsvetanova, K. Croes, N. Jossart, E. Grimaldi, M. Baumgartner, D. Crotti, A. Fumémont, P. Gambardella and G. S. Kar, "SOT-MRAM 300MM Integration for Low Power and Ultrafast Embedded Memories," *2018 IEEE Symposium on VLSI Circuits*, pp. 81-82, 2018.
- [2] S. Manipatruni, D. E. Nikonov, C.-C. Lin, T. A. Gosavi, H. Liu, B. Prasad, Y.-L. Huang, E. Bonturim, R. Ramesh and I. A. Young, "Scalable energy-efficient magnetoelectric spin-orbit logic," *Nature*, vol. 565, p. 35-42, 2019.
- [3] V. T. Pham, I. Groen, S. Manipatruni, W. Y. Choi, D. E. Nikonov, E. Sagasta, C.-C. Lin, T. A. Gosavi, A. Marty, L. E. Hueso, I. A. Young and F. Casanova, "Spin-orbit magnetic state readout in scaled ferromagnetic/heavy metal nanostructures," *Nature Electronics*, vol. 3, p. 309-315, 2020.
- [4] J. Sinova, S. O. Valenzuela, J. Wunderlich, C. H. Back and T. Jungwirth, "Spin Hall effects," *Review of Modern Physics*, vol. 87, p. 1213, 2015.
- [5] A. Manchon, H. C. Koo, J. Nitta, S. M. Frolov and R. A. Duine, "New perspectives for Rashba spin-orbit coupling," *Nature Materials*, vol. 14, p. 871-882, 2015.
- [6] T. Kimura, Y. Otani, T. Sato, S. Takahashi and S. Maekawa, "Room-Temperature Reversible Spin Hall Effect," *Physical Review Letters*, vol. 98, p. 156601, 2007.
- [7] C. Sanz-Fernández, V. T. Pham, E. Sagasta, L. E. Hueso, I. V. Tokatly, F. Casanova and F. S. Bergeret, "Quantification of interfacial spin-charge conversion in hybrid devices with a metal/insulator interface," *Applied Physics Letters*, vol. 117, p. 142405, 2020.
- [8] I. M. Miron, K. Garello, G. Gaudin, P.-J. Zermatten, M. V. Costache, S. Auffret, S. Bandiera, B. Rodmacq, A. Schuhl and P. Gambardella, "Perpendicular switching of a single ferromagnetic layer induced by in-plane current injection," *Nature*, vol. 476, p. 189-193, 2011.
- [9] L. Liu, C.-F. Pai, Y. Li, H. W. Tseng, D. C. Ralph and R. A. Buhrman, "Spin-Torque Switching with the Giant Spin Hall Effect of Tantalum," *Science*, vol. 336, no. 6081, pp. 555-558, 2012.
- [10] A. R. Mellnik, J. S. Lee, A. Richardella, J. L. Grab, P. J. Mintun, M. H. Fischer, A. Vaezi, A. Manchon, E.-A. Kim, N. Samarth and D. C. Ralph, "Spin-transfer torque generated by a topological insulator," *Nature*, vol. 511, pp. 449-451, 2014.
- [11] Y. Fan, P. Upadhyaya, X. Kou, M. Lang, S. Takei, Z. Wang, J. Tang, L. He, L.-T. Chang, M. Montazeri, G. Yu, W. Jiang, T. Nie, R. N. Schwartz, Y. Tserkovnyak and K. L. Wang, "Magnetization switching through giant spin-orbit torque in a magnetically doped topological insulator heterostructure," *Nature Materials*, vol. 13, p. 699-704, 2014.
- [12] A. Avsar, H. Ochoa, F. Guinea, B. Özyilmaz, B. J. van Wees and I. J. Vera-Marun, "Colloquium: Spintronics in graphene and other two-dimensional materials," *Review of Modern Physics*, vol. 92, p. 021003, 2020.
- [13] W. Han, R. K. Kawakami, M. Gmitra and J. Fabian, "Graphene spintronics," *Nature Nanotechnology*, vol. 9, pp. 794-807, 2014.

- [14] A. K. Geim and I. V. Grigorieva, "Van der Waals heterostructures," *Nature*, vol. 499, pp. 419-425, 2013.
- [15] J. F. Sierra, J. Fabian, R. K. Kawakami, S. Roche and S. O. Valenzuela, "Van der Waals heterostructures for spintronics and opto-spintronics," *Nature Nanotechnology*, vol. 16, pp. 856-868, 2021.
- [16] J. H. Garcia, A. W. Cummings and S. Roche, "Spin Hall Effect and Weak Antilocalization in Graphene/Transition Metal Dichalcogenide Heterostructures," *Nano Letters*, vol. 17, no. 8, p. 5078–5083, 2017.
- [17] M. Milletari, M. Offidani, A. Ferreira and R. Raimondi, "Covariant Conservation Laws and the Spin Hall Effect in Dirac-Rashba Systems," *Physical Review Letters*, vol. 119, p. 246801, 2017.
- [18] J. H. Garcia, M. Vila, A. W. Cummings and S. Roche, "Spin transport in graphene/transition metal dichalcogenide heterostructures," *Chemical Society Reviews*, vol. 47, pp. 3359-3379, 2018.
- [19] M. Offidani, M. Milletari, R. Raimondi and A. Ferreira, "Optimal Charge-to-Spin Conversion in Graphene on Transition-Metal Dichalcogenides," *Physical Review Letters*, vol. 119, p. 196801, 2017.
- [20] C. K. Safeer, J. Ingla-Aynés, F. Herling, J. H. Garcia, M. Vila, N. Ontoso, M. Reyes Calvo, S. Roche, L. E. Hueso and F. Casanova, "Room-Temperature Spin Hall Effect in Graphene/MoS₂ van der Waals Heterostructures," *Nano Letters*, vol. 19, no. 2, pp. 1074-1082, 2019.
- [21] L. A. Benítez, W. Savero Torres, J. F. Sierra, M. Timmermans, J. H. Garcia, S. Roche, M. V. Costache and S. O. Valenzuela, "Tunable room-temperature spin galvanic and spin Hall effects in van der Waals heterostructures," *Nature Materials*, vol. 19, pp. 170-175, 2020.
- [22] F. Herling, C. K. Safeer, J. Ingla-Aynés, N. Ontoso, L. E. Hueso and F. Casanova, "Gate tunability of highly efficient spin-to-charge conversion by spin Hall effect in graphene proximitized with WSe₂," *APL Materials*, vol. 8, no. 7, p. 071103, 2020.
- [23] T. S. Ghiasi, A. A. Kaverzin, P. J. Blah and B. J. van Wees, "Charge-to-Spin Conversion by the Rashba–Edelstein Effect in Two-Dimensional van der Waals Heterostructures up to Room Temperature," *Nano Letters*, vol. 19, no. 9, p. 5959–5966, 2019.
- [24] C. K. Safeer, N. Ontoso, J. Ingla-Aynés, F. Herling, V. T. Pham, A. Kurzmann, K. Ensslin, A. Chuvilin, I. Robredo, M. G. Vergniory, F. de Juan, L. E. Hueso, M. Reyes Calvo and F. Casanova, "Large Multidirectional Spin-to-Charge Conversion in Low-Symmetry Semimetal MoTe₂ at Room Temperature," *Nano Letters*, vol. 19, no. 12, pp. 8758-8766, 2019.
- [25] B. Zhao, B. Karpik, D. Khokhriakov, A. Johansson, A. Md Hoque, X. Xu, Y. Jiang, I. Mertig and S. P. Dash, "Unconventional Charge–Spin Conversion in Weyl-Semimetal WTe₂," *Advanced Materials*, vol. 32, p. 2000818, 2020.
- [26] L. Camosi, J. Světlík, M. V. Costache, W. Savero Torres, I. Fernández Aguirre, V. Marinova, D. Dimitrov, M. Gospodinov, J. F. Sierra and S. O. Valenzuela, "Resolving spin currents and spin densities generated by charge-spin interconversion in systems with reduced crystal symmetry," *2D Materials*, vol. 9, no. 3, p. 035014, 2022.

- [27] J. Ingla-Aynés, I. Groen, F. Herling, N. Ontoso, C. K. Safeer, F. de Juan, L. E. Hueso, M. Gobbi and F. Casanova, "Omnidirectional spin-to-charge conversion in graphene/NbSe₂ van der Waals heterostructures," *2D Materials*, vol. 9, no. 4, p. 045001, 2022.
- [28] N. Ontoso, C. K. Safeer, F. Herling, J. Ingla-Aynés, H. Yang, Z. Chi, B. Martin-Garcia, I. Robredo, M. G. Vergniory,, F. de Juan, M. Reyes Calvo, L. E. Hueso and F. Casanova, "Unconventional Charge-to-Spin Conversion in Graphene/MoTe₂ van der Waals Heterostructures," *Physical Review Applied*, vol. 19, p. 014053, 2023.
- [29] T. Naimer, K. Zollner, M. Gmitra and J. Fabian, "Twist-angle dependent proximity induced spin-orbit coupling in graphene/transition metal dichalcogenide heterostructures," *Physical Review B*, vol. 104, p. 195156, 2021.
- [30] A. Veneri, D. T. S. Perkins, C. G. Péterfalvi and A. Ferreira, "Twist angle controlled collinear Edelstein effect in van der Waals heterostructures," *Physical Review B*, vol. 106, p. L081406, 2022.
- [31] S. Lee, D. J. P. de Sousa, Y.-K. Kwon, F. de Juan, Z. Chi, F. Casanova and T. Low, "Charge-to-spin conversion in twisted graphene / WSe₂ heterostructures," *Physical Review B*, vol. 106, p. 165420, 2022.
- [32] K. Szałowski, M. Milivojevic, D. Kochan and M. Gmitra, "Spin-orbit and exchange proximity couplings in graphene/1T-TaS₂ heterostructure triggered by a charge density wave," *2D Materials*, vol. 10, p. 025013, 2023.
- [33] R. Comin and A. Damascelli, "Resonant X-Ray Scattering Studies of Charge Order in Cuprates," *Annual Review of Condensed Matter Physics*, vol. 7, pp. 369-405, 2016.
- [34] M. Yoshida, Y. Zhang, J. Ye, R. Suzuki, Y. Imai, S. Kimura, A. Fujiwara and Y. Iwasa, "Controlling charge-density-wave states in nano-thick crystals of 1T-TaS₂," *Scientific Reports*, vol. 4, p. 7302, 2014.
- [35] Y. Ma, D. Wu, C. Lu and C. Petrovic, "The electric pulses induced multi-resistance states in the hysteresis temperature range of 1T-TaS₂ and 1T-TaS_{1.6}Se_{0.4}," *Applied Physics Letters*, vol. 116, p. 171906, 2020.
- [36] G. Liu, T. Qiu, K. He, Y. Liu, D. Lin, Z. Ma, Z. Huang, W. Tang, J. Xu, K. Watanabe, T. Taniguchi, L. Gao, J. Wen, J.-M. Liu, B. Yan and X. Xi, "Electrical switching of ferro-rotational order in nanometre-thick 1T-TaS₂ crystals," *Nature Nanotechnology*, 2023.
- [37] F. Zwick, H. Berger, I. Vobornik, G. Margaritondo, L. Forró, C. Beeli, M. Onellion, G. Panaccione, A. Taleb-Ibrahim and M. Grioni, "Spectral Consequences of Broken Phase Coherence in 1T-TaS₂," *Physical Review Letters*, vol. 81, no. 5, p. 1058–1061, 1998.
- [38] W. Yan, E. Sagasta, M. Ribeiro, Y. Niimi, L. E. Hueso and F. Casanova, "Large room temperature spin-to-charge conversion signals in a few-layer graphene/Pt lateral heterostructure," *Nature Communications*, vol. 8, p. 661, 2017.
- [39] C. K. Safeer, F. Herling, W. Y. Choi, N. Ontoso, J. Ingla-Aynés, L. E. Hueso and F. Casanova, "Reliability of spin-to-charge conversion measurements in graphene-based lateral spin valves," *2D Materials*, vol. 9, no. 1, p. 015024, 2021.

- [40] A. Roy, M. H. D. Guimarães and J. Sławińska, "Unconventional spin Hall effects in nonmagnetic solids," *Physical Review Materials*, vol. 6, p. 045004, 2022.
- [41] H. F. Yang, K. Y. He, J. Koo, S. W. Shen, S. H. Zhang, G. Liu, Y. Z. Liu, C. Chen, A. J. Liang, L. Huang, M. X. Wang, J. J. Gao, X. Luo, L. X. Yang, J. P. Liu, Y. P. Sun, S. C. Yan, B. H. Yan, Y. L. Chen, X. Xi and Z. K. Liu, "Visualization of Chiral Electronic Structure and Anomalous Optical Response in a Material with Chiral Charge Density Waves," *Physical Review Letters*, vol. 129, p. 156401, 2022.
- [42] M. Hirayama, R. Okugaw, S. Murakami and T. Miyake, "Weyl Node and Spin Texture in Trigonal Tellurium and Selenium," *Physical Review Letters*, vol. 114, p. 206401, 2015.
- [43] M. Sakano, M. Hirayama, T. Takahashi, S. Akebi, M. Nakayama, K. Kuroda, K. Taguchi, T. Yoshikawa, K. Miyamoto, T. Okuda, K. Ono, H. Kumigashira, T. Ideue, Y. Iwasa, N. Mitsuishi, K. Ishizaka, S. Shin, T. Miyake, S. Murakami, T. Sasagawa and T. Konda, "Radial Spin Texture in Elemental Tellurium with Chiral Crystal Structure," *Physical Review Letters*, vol. 124, p. 136404, 2020.
- [44] X. L. Wu and C. M. Lieber, "Direct Observation of Growth and Melting of the Hexagonal-Domain Charge-Density-Wave Phase in 1T-TaS₂ by Scanning Tunneling Microscopy," *Physical Review Letters*, vol. 64, pp. 1150-1153, 1990.
- [45] R. Thomson, B. Burk, A. Zettl and J. Clarke, "Scanning tunneling microscopy of the charge-density-wave structure in 1T-TaS₂," *Physical Review B*, vol. 49, p. 16899, 1994.
- [46] Y. Zhao, Z. Nie, H. Hong, X. Qiu, S. Han, Y. Yu, M. Liu, X. Qiu, K. Liu, S. Meng, L. Tong and J. Zhang, "Spectroscopic visualization and phase manipulation of chiral charge density waves in 1T-TaS₂," *Nature Communications*, vol. 14, p. 2223, 2023.
- [47] M. Yoshida, R. Suzuki, Y. Zhang, M. Nakano and Y. Iwasa, "Memristive phase switching in two-dimensional 1T-TaS₂ crystals," *Science Advances*, vol. 1, no. 9, p. e1500606, 2015.
- [48] W. Yan, O. Txoperena, R. Llopis, H. Dery, L. E. Hueso and F. Casanova, "A two-dimensional spin field-effect switch," *Nature Communications*, vol. 7, p. 13372, 2016.
- [49] D. MacNeill, G. M. Stiehl, M. H. D. Guimarães, R. A. Buhrman, J. Park and D. C. Ralph, "Control of spin-orbit torques through crystal symmetry in WTe₂/ferromagnet bilayers," *Nature Physics*, vol. 13, pp. 300-305, 2017.
- [50] I.-H. Kao, R. Muzzio, H. Zhang, M. Zhu, J. Gobbo, S. Yuan, D. Weber, R. Rao, J. Li, J. H. Edgar, J. E. Goldberger, J. Yan, D. G. Mandrus, J. Hwang, R. Cheng, J. Katoch and S. Singh, "Deterministic switching of a perpendicularly polarized magnet using unconventional spin-orbit torques in WTe₂," *Nature Materials*, vol. 21, p. 1029-1034, 2022.
- [51] D. d. Sousa, P. Haney, J. Wang and T. Low, "Field-Free-Switching State Diagram of Perpendicular Magnetization Subjected to Conventional and Unconventional Spin-Orbit Torques," *Physical Review Applied*, vol. 18, p. 054020, 2022.
- [52] L. Liu, C. Zhou, X. Shu, C. Li, T. Zhao, W. Lin, J. Deng, Q. Xie, S. Chen, J. Zhou, R. Guo, H. Wang, J. Yu, S. Shi, P. Yang, S. Pennycook, A. Manchon and J. Chen, "Symmetry-dependent field-free switching of perpendicular magnetization," *Nature Nanotechnology*, vol. 15, p. 277-282, 2021.

- [53] D. Culcer and R. Winkler, "Generation of Spin Currents and Spin Densities in Systems with Reduced Symmetry," *Physical Review Letters*, vol. 99, p. 226601, 2007.
- [54] W. Khon and L. J. Sham, "Self-Consistent Equations Including Exchange and Correlation Effects," *Physical Review*, vol. 140, p. A1133–A1138, 1965.
- [55] P. Giannozzi et al., "Quantum espresso: a modular and open-source software project for quantum simulations of materials," *Journal of Physics: Condensed Matter*, vol. 21, p. 395502, 2009.
- [56] P. Giannozzi et al., "Advanced capabilities for materials modelling with quantum espresso," *Journal of Physics: Condensed Matter*, vol. 29, p. 465901, 2017.
- [57] J. P. Perdew, K. Burke and M. Ernzerhof, "Generalized Gradient Approximation Made Simple," *Physical Review Letters*, vol. 77, p. 3865–3868, 1996.
- [58] S. Grimme, "Semiempirical GGA-Type Density Functional Constructed with a Long-Range Dispersion Correction," *Journal of Computational Chemistry*, vol. 27, p. 1787–1799, 2006.
- [59] G. Y. Guo, S. Murakami, T.-W. Chen and N. Nagaosa, "Intrinsic spin hall effect in platinum: First-principles calculations," *Physical Review Letters*, vol. 100, p. 096401, 2008.
- [60] A. A. Mostofi et al., "An updated version of wannier90: A tool for obtaining maximally-localised wannier functions," *Computer Physics Communications*, vol. 185, p. 2309–2310, 2017.
- [61] G. Pizzi et al., "Wannier90 as a community code: new features and applications," *Journal of Physics: Condensed Matter*, vol. 32, p. 165902, 2020.
- [62] I. Souza, N. Marzari and D. Vanderbilt, "Maximally localized wannier functions for entangled energy bands," *Physical Review B*, vol. 65, p. 035109, 2001.
- [63] J. Qiao, J. Zhou, Z. Yuan and W. Zhao, "Calculation of intrinsic spin hall conductivity by wannier interpolation," *Physical Review B*, vol. 98, p. 214402, 2018.
- [64] S. H. Jo, T. Chang, I. Ebong, B. B. Bhadviya, P. Mazumder and W. Lu, "Nanoscale Memristor Device as Synapse in Neuromorphic Systems," *Nano Letters*, vol. 10, p. 1297–1301, 2010.
- [65] P. Merolla, J. Arthur, R. Alvarez-Icaza, A. Cassidy, J. Sawada, F. Akopyan, B. Jackson, N. Imam, C. Guo, Y. Nakamura, B. Brezzo, I. Vo, S. Esser, R. Appuswamy, B. Taba, A. Amir, M. Flickner, W. Risk, R. Manohar and D. Modha, "A million spiking-neuron integrated circuit with a scalable communication network and interface," *Science*, vol. 345, pp. 668-673, 2014.

Supplementary Information for

Control of charge-spin interconversion in van der Waals heterostructures with chiral charge density waves

Zhendong Chi^{1*}, Seungjun Lee^{2*}, Haozhe Yang^{1*}, Eoin Dolan¹, C. K. Safeer^{1,3}, Josep Ingla-Aynés¹, Franz Herling¹, Nerea Ontoso¹, Beatriz Martín-García^{1,4}, Marco Gobbi^{4,5}, Tony Low^{2,6}, Luis E. Hueso^{1,4}, Fèlix Casanova^{1,4,†}

¹CIC nanoGUNE BRTA, 20018 Donostia-San Sebastián, Basque Country, Spain

²Department of Electrical and Computer Engineering, University of Minnesota, Minneapolis, Minnesota 55455, USA

³Department of Physics, Clarendon Laboratory, University of Oxford, OX13PU, Oxford, United Kingdom

⁴IKERBASQUE, Basque Foundation for Science, 48009 Bilbao, Basque Country, Spain

⁵Centro de Física de Materiales (CSIC-EHU/UPV) and Materials Physics Center (MPC), 20018 Donostia-San Sebastián, Basque Country, Spain

⁶Department of Physics, University of Minnesota, Minneapolis, Minnesota 55455, USA

*These authors equally contributed to this work.

†E-mail: f.casanova@nanogune.eu

Note 1. Atomic force microscopy characterization on 1T-TaS₂

Note 2. Electrical transport of 1T-TaS₂ in Devices 2&3

Note 3. Raman spectroscopy characterization on the graphene in Devices 1&2

Note 4. Gate-voltage dependent transport in Device 1

Note 5. Spin transport characterization

Note 6. Raw data of the CSI characterization on Devices 1&2

Note 7. H_y dependent CSI hysteresis loops in Devices 1 & 2

Note 8. CSI characterization on Device 3

Note 9. First-principles calculations details

Note 1. Atomic force microscopy characterization of 1T-TaS₂

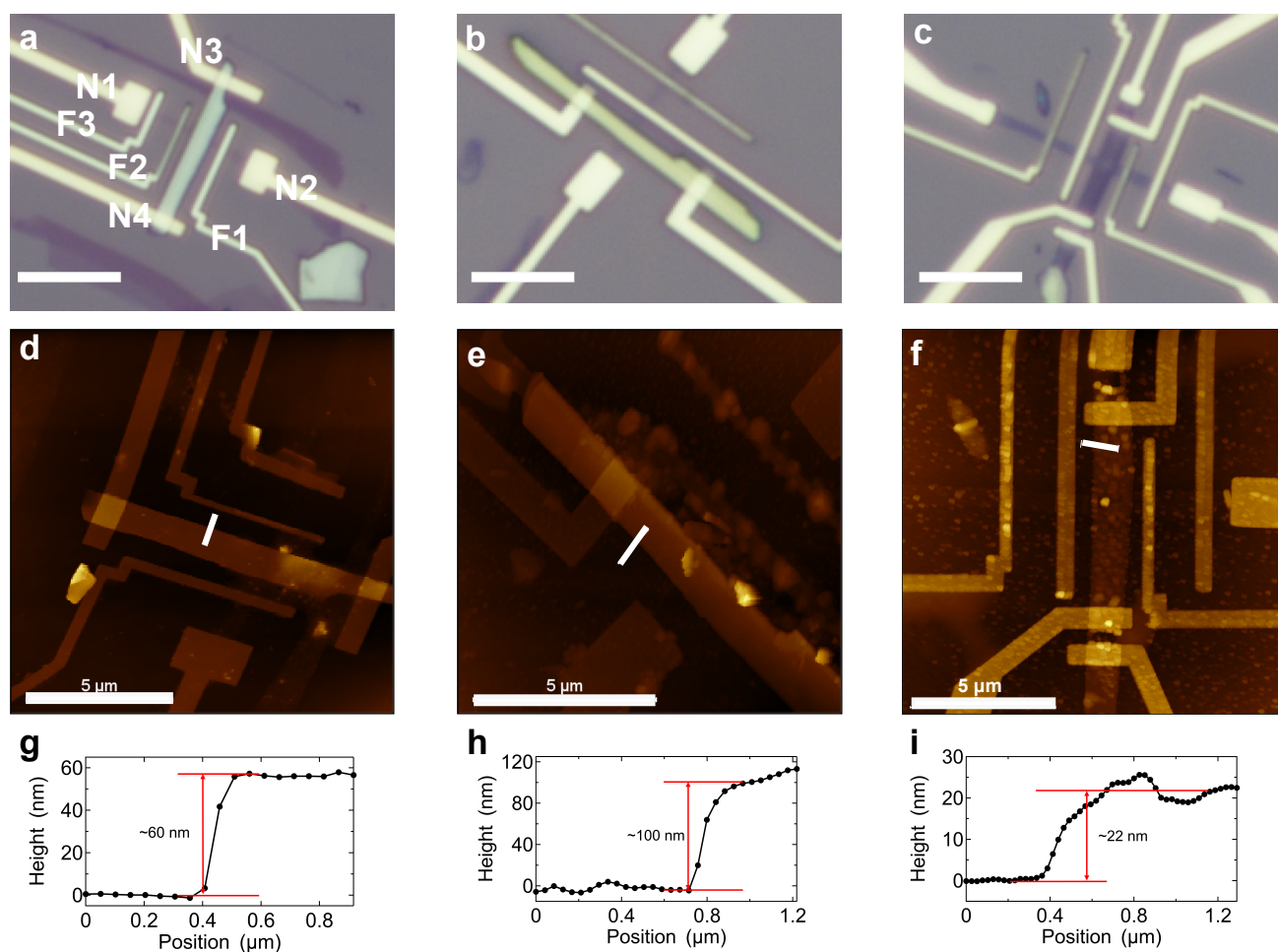


Figure S1. a-c, Optical images of Devices 1 (a), 2 (b), and 3 (c). Scale bar: 5 μm . The ferromagnetic (FM) electrodes (F1 to F3 on Gr) and non-magnetic (NM) electrodes (N1 and N2 on Gr, N3 and N4 on 1T-TaS₂) in Device 1 are labelled. d-f, Atomic force microscopy (AFM) images of Devices 1 (d), 2 (e), and 3 (f). g-i, The height profiles along the white lines drawn in d-f. The thicknesses of the 1T-TaS₂ flakes in the corresponding devices are tagged, as 60 nm (Device 1), 100 nm (Device 2), and 22 nm (Device 3).

Note 2. Electrical transport of 1T-TaS₂ in Devices 2 and 3

The temperature dependence of the resistance of 1T-TaS₂ flake in the three devices is illustrated in Fig.1b in the main text (Device 1) and Fig. S2 (Devices 2 and 3). The data were collected using the two-points measurement method, e.g., between electrodes N3 and N4 in Device 1 (schematically displayed in Fig. S2c). Three resistance levels with two temperature hysteresis loops are observed below 360 K in Devices 1 and 2, which correspond to the ICCDW, NCCDW, CCDW phases and their phase transitions. The NCCDW-CCDW transition in Device 1 was stimulated by applying an in-plane high voltage to 1T-TaS₂ at 120 K [1]. In Device 3, only the ICCDW and NCCDW phases are observed in the 22-nm-thick 1T-TaS₂ flake. These results are in good agreement with previous studies, which have shown that the high-resistive CCDW phase disappears in thin (<40 nm) 1T-TaS₂ flakes [1] [2] [3] [4].

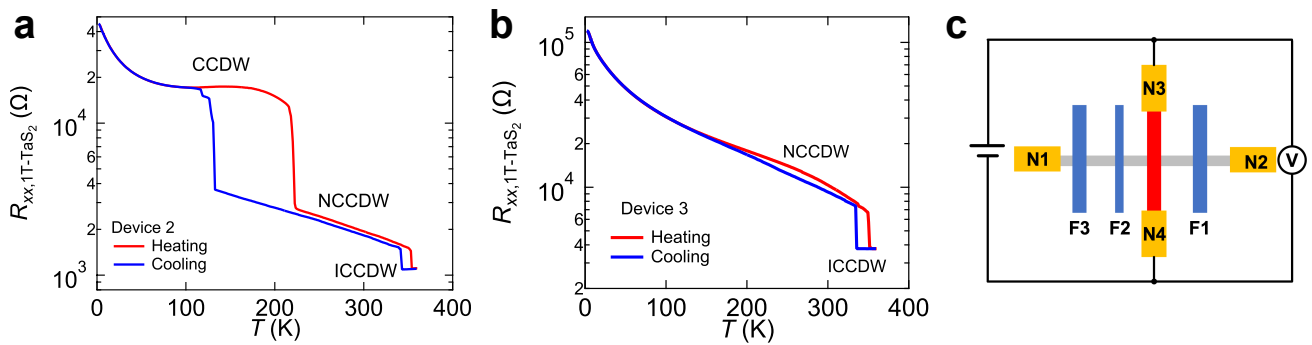


Figure S2. Temperature dependence of the longitudinal resistance of 1T-TaS₂ flakes ($R_{xx,1T-TaS_2}$) in Devices 2 (a) and 3 (b). The heating and cooling processes are illustrated by the red and blue lines, respectively. The different CDW phases in the hysteresis loops are labeled. c, the sketch of the measurement geometry in Device 1.

Note 3. Raman spectroscopy characterization on the graphene in Devices 1 and 2

The number of graphene layers in Devices 1 and 2 is confirmed by using Raman spectroscopy (Alpha 300R Confocal Raman WITec microscope) with a 532 nm laser as excitation source, a diffraction grating of 600 1/nm, and 100× objective lens. Figure S3a illustrates the Raman spectra of the graphene in Devices 1 (red) and 2 (blue) in the range from 1400 to 2900 cm^{-1} . The spectra exhibit clear G and 2D graphene characteristic peaks. The Raman spectra zooming in the 2D peak range in Devices 1 and 2 are shown in Figs. S3b and S3c, respectively. The graphene 2D peak in Device 1 can be fitted well using four Lorentzians, indicating that it is a bilayer [5]. The graphene 2D peak in Device 2 can be fitted well using a single Lorentzian, suggesting that in this case it is a monolayer.

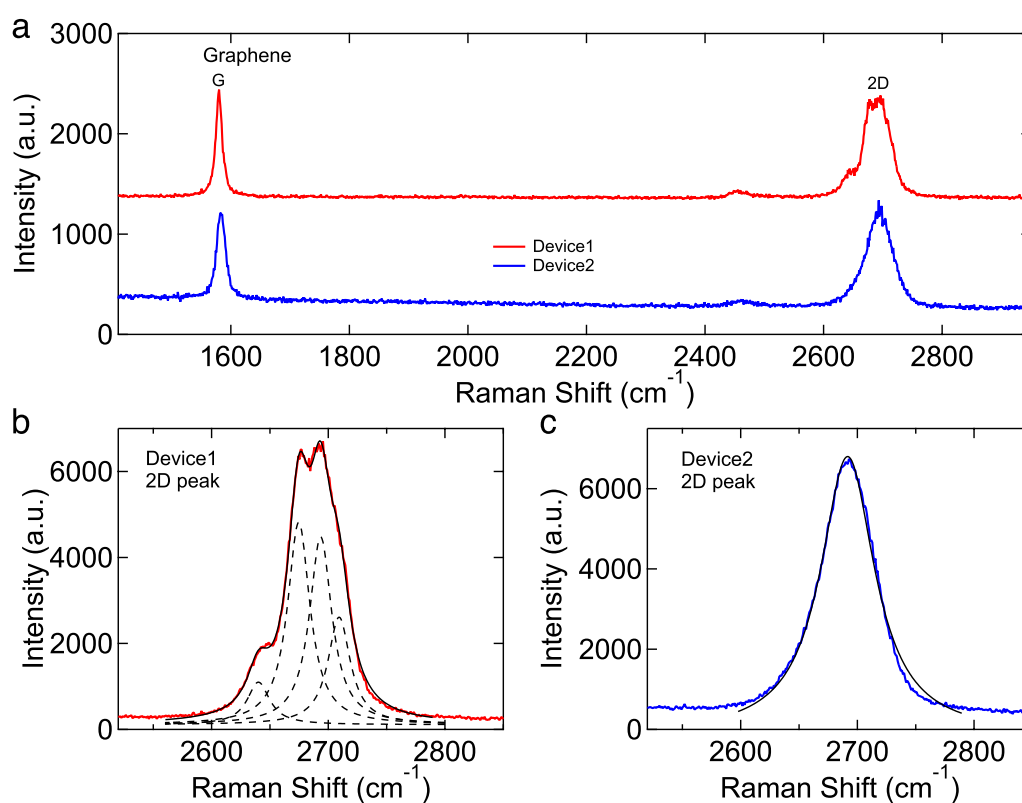


Figure S3. Raman spectra of the graphene in Devices 1 and 2. a, Raman spectra of the graphene in Devices 1 (red) and 2 (blue) showing the G and 2D peaks. b, c, Detailed Raman spectra in the 2D peak range in Devices 1 (b) and 2 (c). The black dashed curves in b represent the four Lorentzians used to fit the 2D peak, and the solid line is the sum of the four Lorentzians. The black solid line in c is the single Lorentzian fitting of the 2D peak of the graphene in Device 2.

Note 4. Gate-voltage dependent transport in Device 1

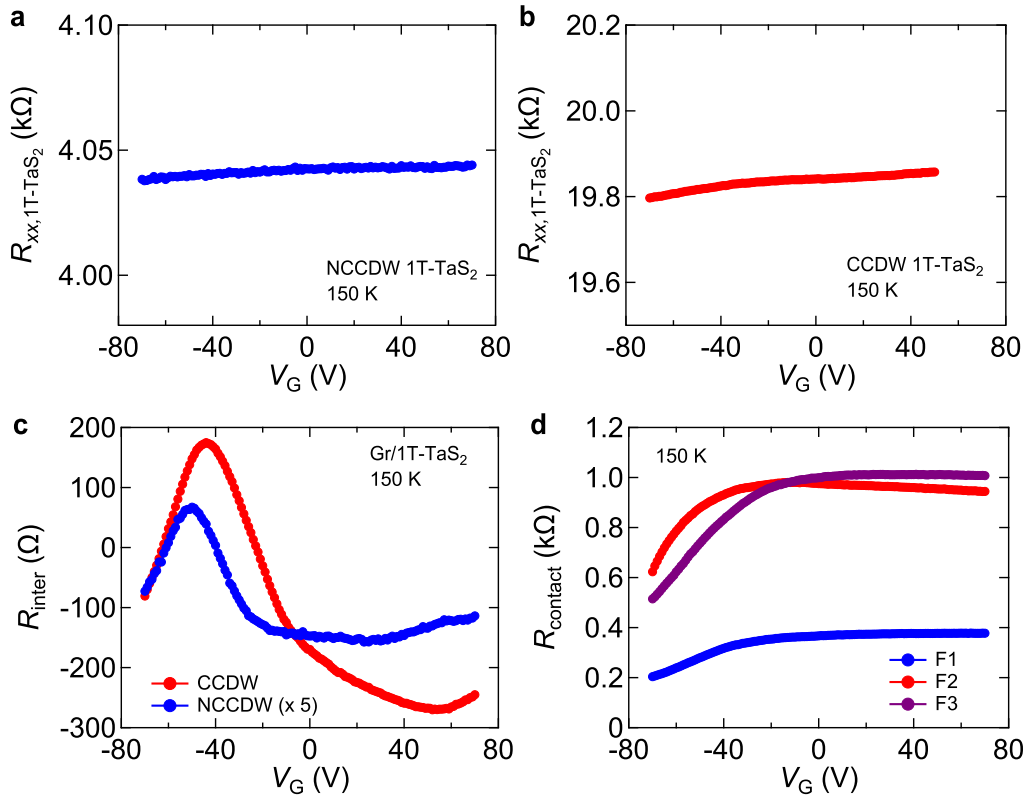


Figure S4. Gate voltage (V_G) dependence of transport properties of graphene/1T-TaS₂ heterostructure in Device 1. a, b, V_G -dependent longitudinal resistance of 1T-TaS₂ ($R_{xx,1T-TaS_2}$) in the NCCDW (a) and CCDW (b) phases. Two-point measurements carried out between N3 and N4 electrodes (see labels in Fig. S1a). c, V_G -dependent graphene/1T-TaS₂ interface resistance (R_{inter}). Four-point measurements were carried by adding a dc current between N4 and N2 electrodes and detecting the voltage between N1 and N3 electrodes (See labels in Fig. S1a). Red and blue curves represent 1T-TaS₂ in the CCDW and NCCDW phases, respectively. Blue curve is displayed by multiplying a factor of 5. d, V_G -dependence of the contact resistance ($R_{contact}$) of the three ferromagnetic electrodes F1 (blue), F2 (red), and F3 (purple). Three-point measurements were carried out by applying a dc current between N1 and F1 (F2, F3) electrodes and detecting the voltage between N2 and F1 (F2, F3) electrodes (See labels in Fig. S1a). V_G -dependent longitudinal resistance of Gr/1T-TaS₂ heterostructure ($R_{xx,cross}$) has been displayed in Fig. 4c in the main text. Four-point measurements were carried out by applying a dc current between electrodes N1 and N2 and detecting the voltage between F2 and F1 electrodes (see labels in Fig. S1a). $R_{xx,cross}$ is lower when 1T-TaS₂ is in the CCDW phase compared to that in the NCCDW phase, which agrees with a recent report [6]. All measurements were carried out at 150 K.

Note 5. Spin transport characterization

The spin injection efficiency from the FM electrodes to Gr is characterized by using the lateral spin valve defined by two FM electrodes on Gr [7] [8] [9]. We measure the non-local resistance R_{NL} for pristine Gr and Gr/1T-TaS₂ heterostructures using two FM electrodes without and with a 1T-TaS₂ flake placed between them, respectively (e.g., F2 and F3, F1 and F2 in Device 1). R_{NL} of the lateral spin valve with pristine Gr in Device 1 measured at 100 K is plotted as a function of H_y in Fig. S5a, showing a clear difference between the parallel ($\uparrow\uparrow$) and antiparallel ($\uparrow\downarrow$) configurations of the two FM electrodes. The non-local spin valve signal is defined as $\Delta R_{\text{LSV}} = R_{\text{NL}}^{\uparrow\uparrow} - R_{\text{NL}}^{\uparrow\downarrow}$, and Fig. S5b shows that ΔR_{LSV} of pristine Gr in Device 1 changes weakly with temperature.

R_{NL} of the lateral spin valve across the Gr/1T-TaS₂ heterostructure in Device 1 measured at 150 K and without gate voltage is plotted as a function of H_y in Fig. S5d. R_{NL} measured when 1T-TaS₂ is in the NCCDW and CCDW phases are represented by the blue and red curves, respectively. We find that ΔR_{LSV} is almost zero in the NCCDW 1T-TaS₂ phase, while R_{NL} shows a clear difference for $\uparrow\uparrow$ and $\uparrow\downarrow$ configurations in the CCDW 1T-TaS₂ phase, due to different spin absorption between these two phases. ΔR_{LSV} in the Gr/CCDW 1T-TaS₂ heterostructure is measured as a function of V_G at 150 K and has been displayed in Fig. 4d in the main text.

Hanle precession is also measured as a function of H_x for pristine Gr (Fig. S5c) and Gr/CCDW 1T-TaS₂ heterostructure (Fig. S5e) in Device 1. However, the oscillation of R_{NL} due to precession (both in $\uparrow\uparrow$ and $\uparrow\downarrow$ configurations) is partially overlapped with magnetization saturation, making an accurate fitting of spin transport parameters difficult. This is caused by the fact that the two FM electrodes used in the measurement are too close ($\sim 2 \mu\text{m}$).

The characterization of the spin injection efficiency of Devices 2 and 3 is presented in Fig. S6. Figures S6a and S6b illustrate R_{NL} of a lateral spin valve with pristine Gr measured at 300 K for Device 2 and Device 3, respectively. The temperature dependence of ΔR_{LSV} in Device 3 is shown in Fig. S6c. Notably, ΔR_{LSV} in these two devices are significantly larger than that observed in Device 1 (Figs. S5a and S5b), indicating a larger spin injection efficiency. ΔR_{LSV} of pristine Gr in Device 3 measured at 50 K as a function of V_G is plotted in Fig. S6d. ΔR_{LSV} exhibits the opposite trend as a function of V_G than the resistance of Gr, which is consistent with the behavior observed in Device 1 (Figs. 4c and 4d in the main text).

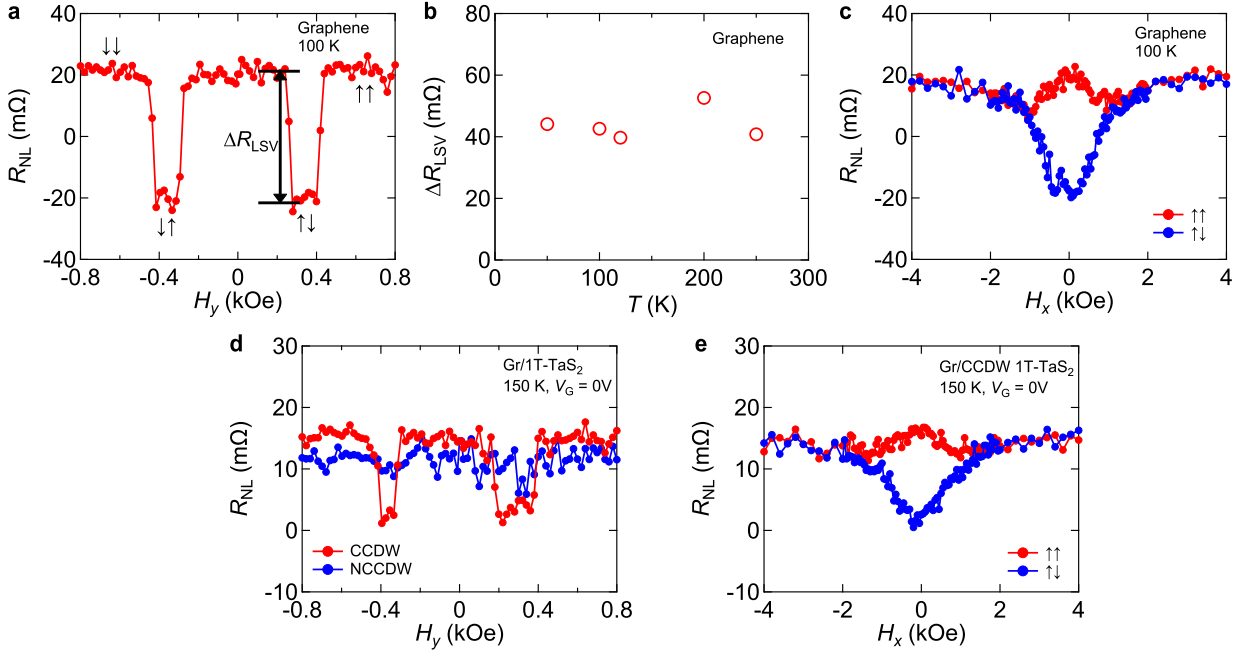


Figure S5. Spin transport characterization on Device 1. a, Non-local resistance (R_{NL}) of the lateral spin valve with pristine Gr measured as a function of H_y at 100 K. \uparrow and \downarrow indicate the magnetization directions of the two FM electrodes used in the non-local spin valve measurement. The spin signal is defined as the difference between the parallel and antiparallel states and labeled as ΔR_{LSV} . b, Temperature (T) dependence of ΔR_{LSV} in the lateral spin valve with pristine Gr. c, Hanle precession of the lateral spin valve with pristine Gr measured as a function of H_x at 100 K. $\uparrow\uparrow$ ($\uparrow\downarrow$) represent the parallel (antiparallel) configuration of the two FM electrodes in the lateral spin valve. d, R_{NL} of the lateral spin valve with Gr/1T-TaS₂ heterostructure measured under H_y at 150 K. The red and blue lines represent 1T-TaS₂ in CCDW and NCCDW phases, respectively. e, Hanle precession of the lateral spin valve with Gr/CCDW 1T-TaS₂ heterostructure measured under H_x at 150 K.

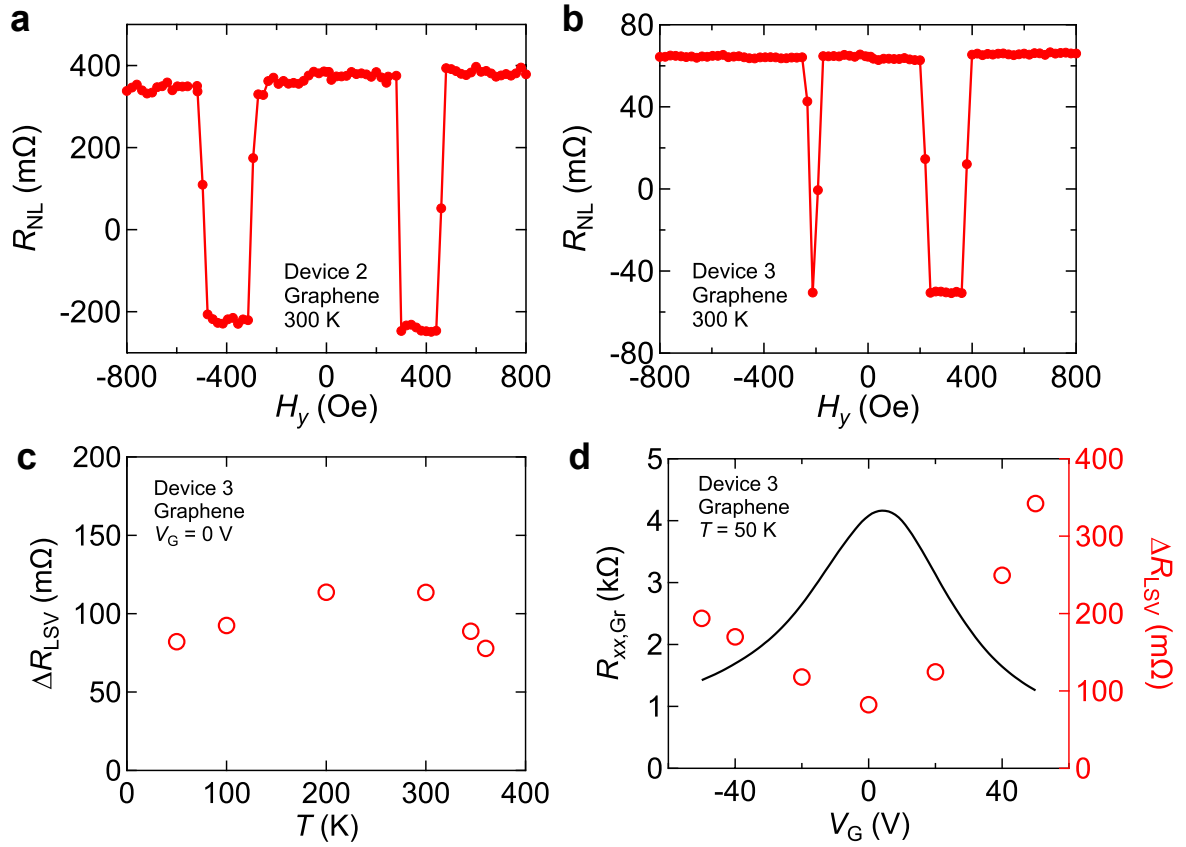


Figure S6. Spin transport characterization on Devices 2 and 3. **a, b,** Non-local resistance R_{NL} of the lateral spin valve with pristine Gr as a function of H_y at 300 K in Devices 2 (**a**) and 3 (**b**). The spin signal is defined as the difference between the parallel and antiparallel states and labeled as ΔR_{LSV} . **c,** Temperature dependence of ΔR_{LSV} in the lateral spin valve with pristine Gr at $V_G = 0$ V in Device 3. **d,** V_G dependence of the resistance ($R_{xx,Gr}$, black curve) and ΔR_{LSV} (red circles) of pristine Gr at 50 K in Device 3.

Note 6. Raw data of the CSI characterization on Devices 1 & 2

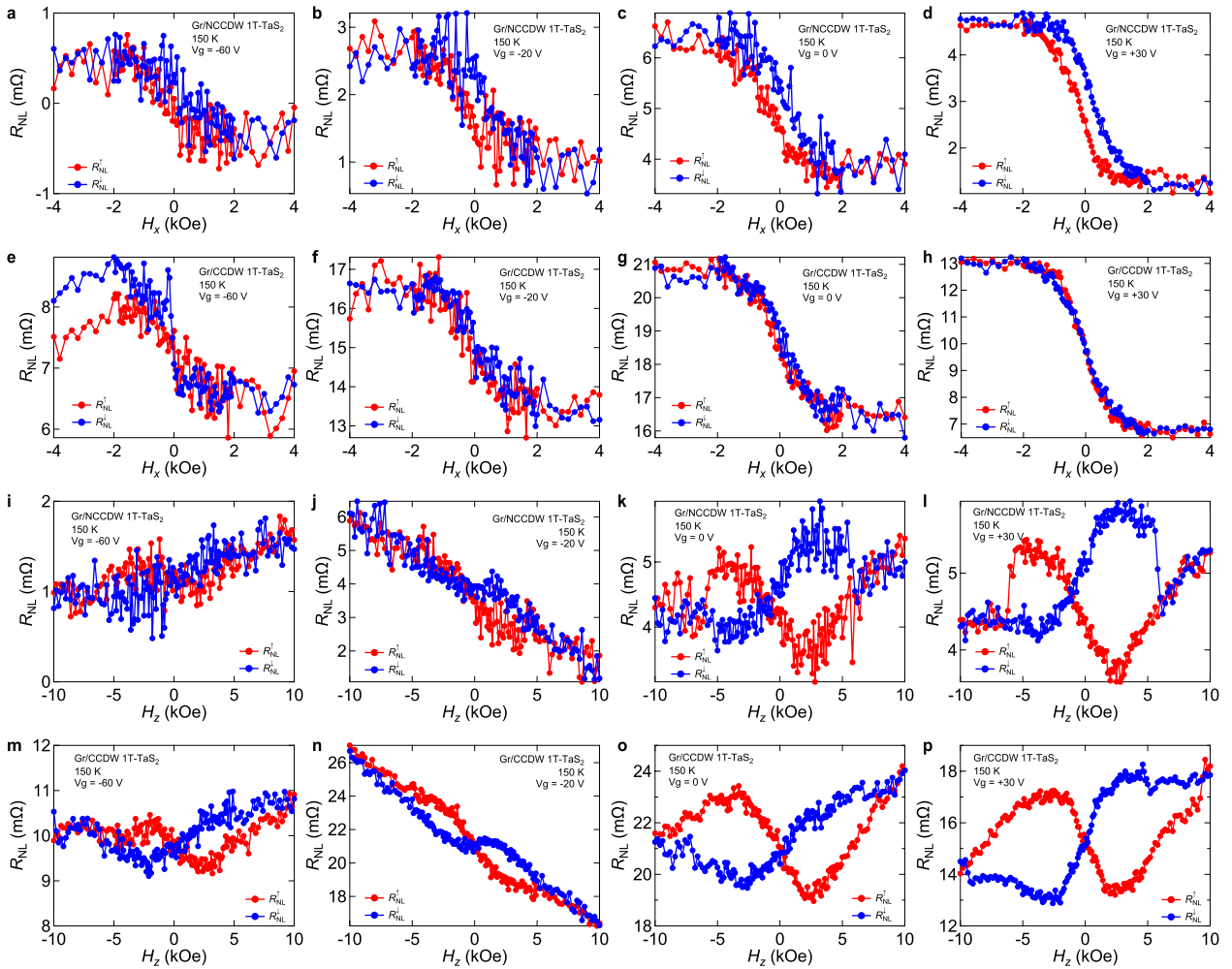


Figure S7. R_{NL} of CSI raw data collected in Device 1 with $V_G = -60, -20, 0,$ and $+30$ V at 150 K. a-d, H_x -dependent R_{NL} in Gr/NCCDW 1T-TaS₂. e-h, H_x -dependent R_{NL} in Gr/CCDW 1T-TaS₂. i-l, H_z -dependent R_{NL} in Gr/NCCDW 1T-TaS₂. m-p, H_z -dependent R_{NL} in Gr/CCDW 1T-TaS₂.

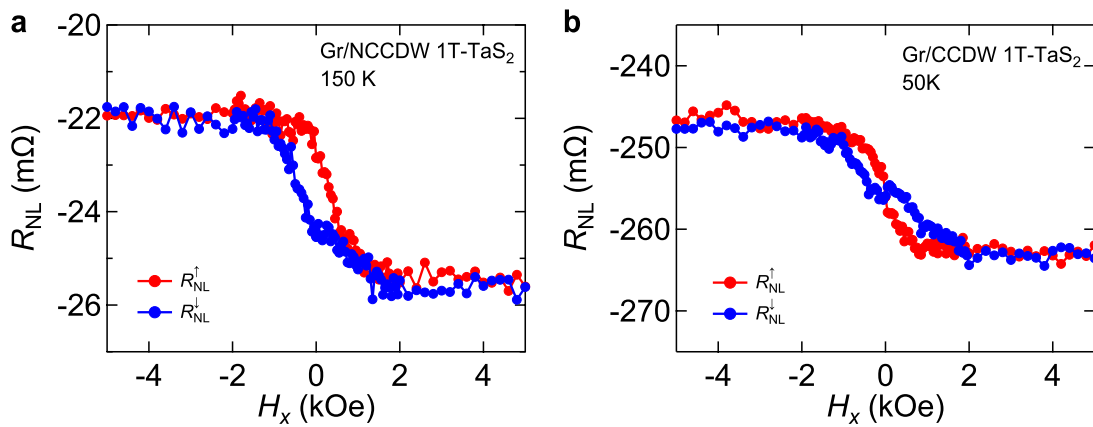


Figure S8. R_{NL} raw data measured in Device 2. a, H_x -dependent R_{NL} in Gr/NCCDW 1T-TaS₂ measured at 150 K and $V_G = 0$ V. b, H_x -dependent R_{NL} in Gr/CCDW 1T-TaS₂ measured at 50 K and $V_G = 0$ V.

Note 7. H_y dependent CSI hysteresis loops in Devices 1 & 2

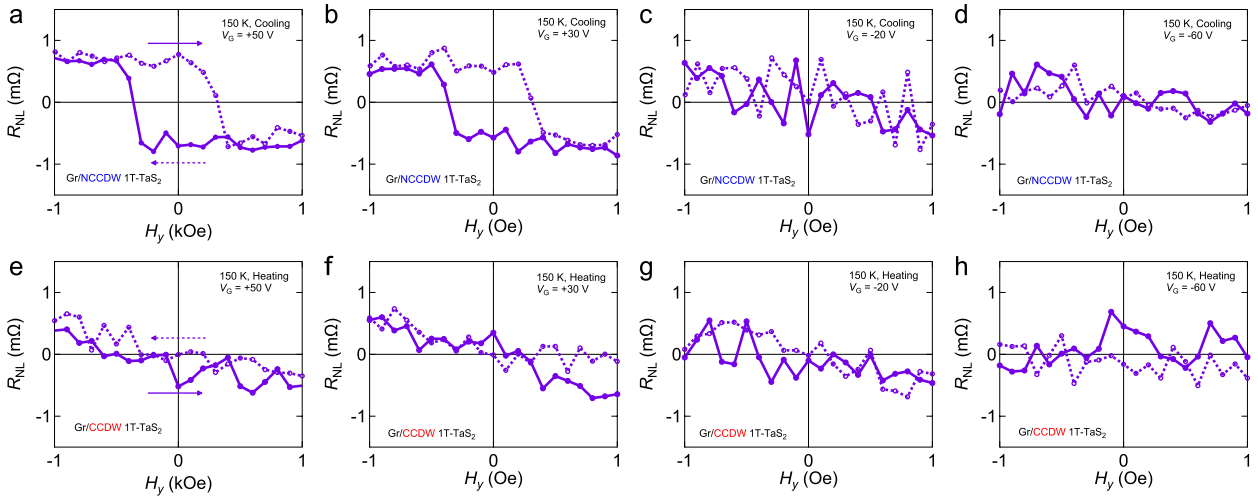


Figure S9. Non-local CSI resistance (R_{NL}) of Device 1 measured as a function of H_y at the NCCDW (a-d) and CCDW (e-h) phases of 1T-TaS₂ with different back gate voltages (V_G). V_G equals +50 (a,e), +30 (b,f), -20 (c,g), and -60 (d,h) V, respectively. The arrows represent the scanning directions of H_y . All the data were obtained at 150 K. A constant baseline has been subtracted from the lines in all the panels.

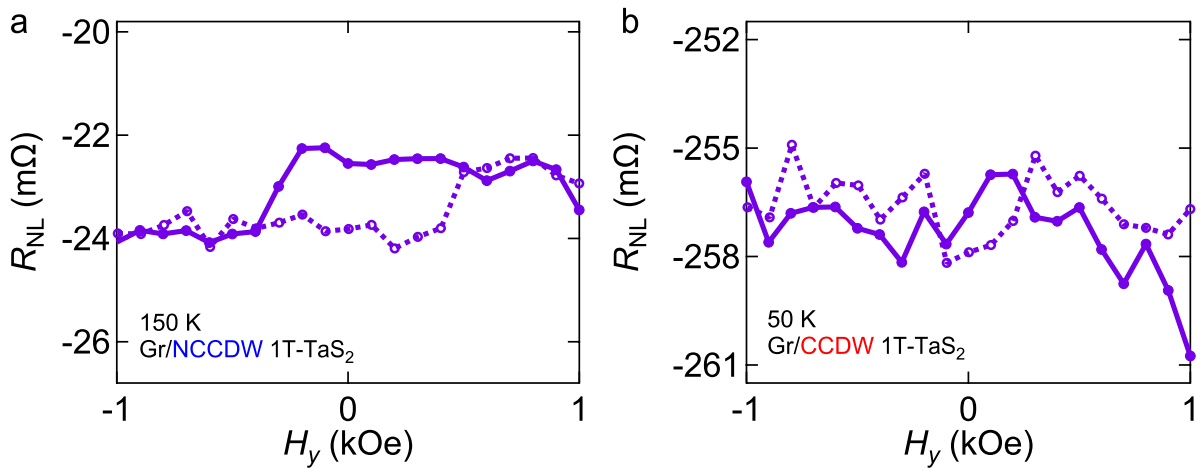


Figure S10. R_{NL} of Device 2 measured as a function of H_y at the NCCDW (a) and CCDW (b) phases of 1T-TaS₂. The measuring temperature is 150 K (a) and 50 K (b), respectively. No back gate voltage was added during the measurement.

Note 8. CSI characterization on Device 3

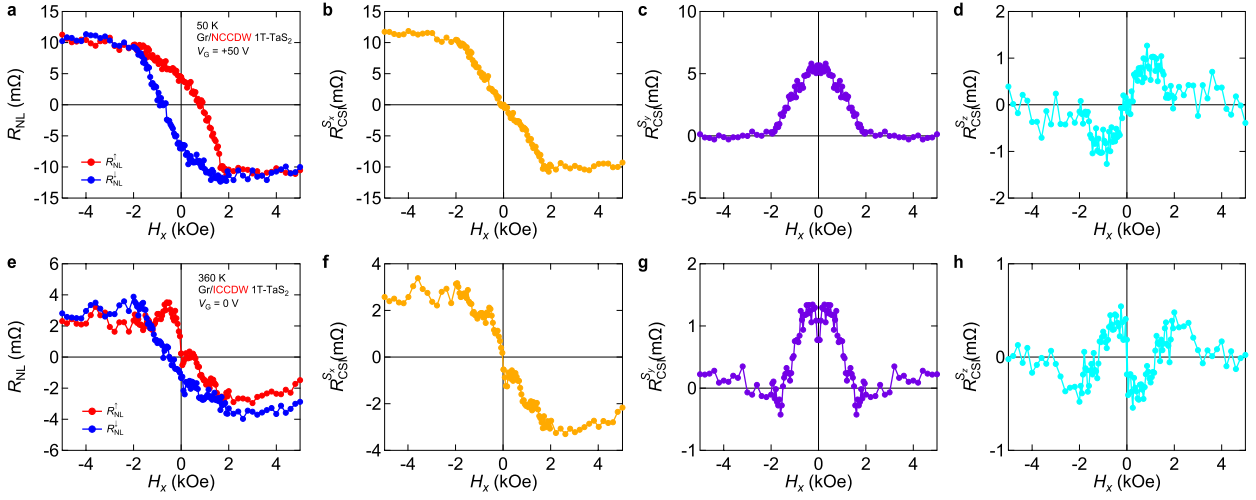


Figure S11. CSI characterization on Device 3. a-d, H_x -dependent R_{NL} (a), $R_{CSI}^{S_x}$ (b), $R_{CSI}^{S_y}$ (c), and $R_{CSI}^{S_z}$ (d) in Gr/NCCDW 1T-TaS₂ heterostructure measured with $V_G = +50$ V at 50 K. e-h, H_x -dependent R_{NL} (e), $R_{CSI}^{S_x}$ (f), $R_{CSI}^{S_y}$ (g), and $R_{CSI}^{S_z}$ (h) in Gr/ICCDW 1T-TaS₂ heterostructure measured with $V_G = 0$ V at 360 K.

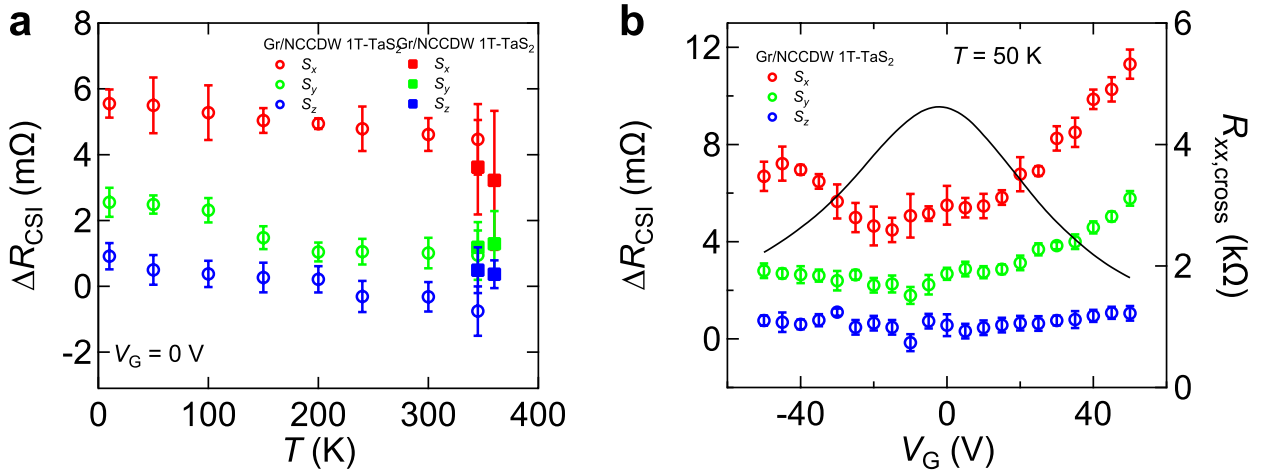


Figure S12. a, Temperature dependence of ΔR_{CSI} induced by S_x (red), S_y (green), and S_z (blue) measured at $V_G = 0$ V. b, Gate voltage dependence of ΔR_{CSI} induced by S_x (red), S_y (green), and S_z (blue) measured at $T = 50$ K. The black line is the resistance of Gr/1T-TaS₂ heterostructure ($R_{xx,cross}$).

Note 9. First-principles calculations details

The equilibrium lattice constants of normal and CCDW states of 1T-TaS₂ were calculated to be $a = 3.356 \text{ \AA}$, $c = 5.792 \text{ \AA}$, and $a = 12.130 \text{ \AA}$, $c = 6.057 \text{ \AA}$, respectively. For the bulk CCDW phase, we only considered the AA stacking configuration. We used a 5×5 supercell structure of graphene to construct a Gr/CCDW 1T-TaS₂ heterostructure as shown in Figure S12. The lattice mismatch between Gr and CCDW 1T-TaS₂ is about 1%. We also used the same size of the supercell for Gr/metallic 1T-TaS₂ heterostructure. Here, the twist-angle between graphene and 1T-TaS₂ is 13.9° .

Initially, we aim to understand the role of the interlayer interaction in the Gr/1T-TaS₂ heterostructure with respect to the CCDW phase. Figures S13a and S13b show their band structures and spin Berry curvature (SBC) along the high symmetry line. Here, the colors represent the conventional SBC components (Ω_{xy}^z). In both cases, Gr is hole doped indicating charge transfer from Gr to 1T-TaS₂. Such a strong interaction leads to an SBC hotspot which is clearly shown in the inset of Figure S13a. Interestingly, in the CCDW phase, SBC hotspots are only observed in the Dirac band (near K points) not in the CDW band. However, in the normal state, not only Dirac bands but also 1T-TaS₂ contribute to SBC hotspots due to its broken symmetry and enhanced perpendicular electric field in 1T-TaS₂ assisted by Gr.

The spin Hall conductivity (SHC) tensor is/was calculated by Kubo formula as described in the Methods section. As a first step, we constructed a Wannier Hamiltonian by using Wannier90 code [10-12]. As shown in Figure S14, our Wannier band structures show excellent agreement with band structures calculated by first-principles calculations. Then, we evaluated the SHC as a function of energy (Figure S14) and constructed the SHC tensors by using the SHC values at the Fermi level (Figure S15).

Although the SHC components are very sensitive to the in-plane rotation, it is very difficult to determine the exact crystallographic orientation of both graphene and 1T-TaS₂ in the experiments. To thoroughly investigate all possibilities, we evaluated crystal-orientation-dependent SHC, as shown in Figure S15, obtained through $\sigma_{[a'_1 a'_2 a'_3]_{ij}}^k = \sum_{lmn} D_{il} D_{jm} D_{kn} \sigma_{[a_1 a_2 a_3]_{lm}}^n$, where D is a rotation matrix and $a_1 a_2 a_3$ and $a'_1 a'_2 a'_3$ indicate crystal orientation before and after rotation [13] [14]. Then, the final SHC components represented in Table 1 of the main text are/were chosen from Figure S14 giving a maximum value of each component.

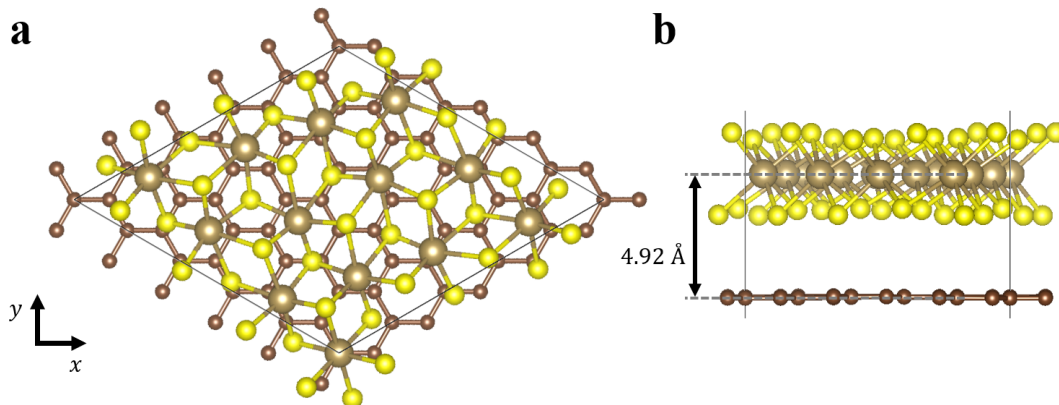


Figure S13. Crystal structure of Gr/CCDW 1T-TaS₂ heterostructure. a, top and b, side view of heterobilayer. Gold, yellow, and brown spheres indicate Ta, S, and C atoms, respectively.

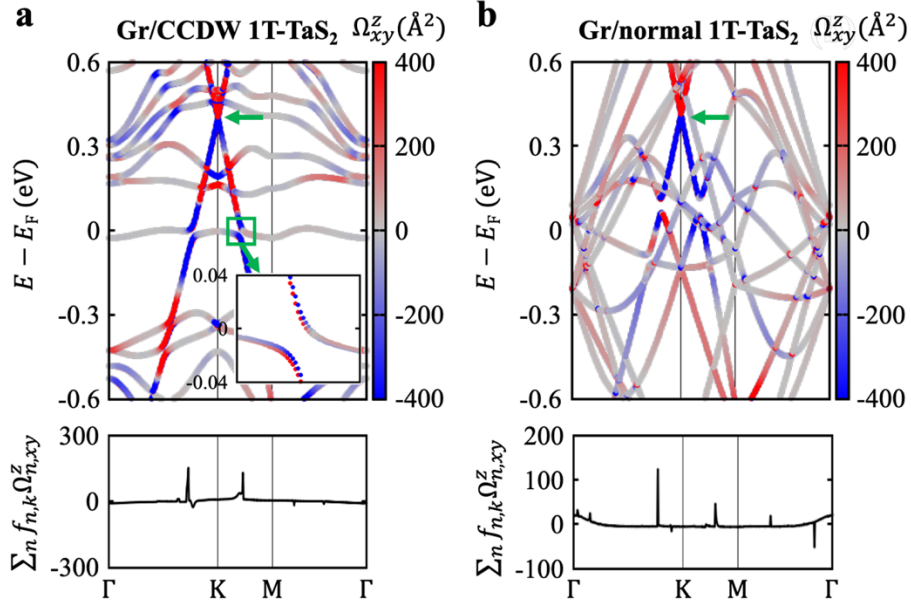


Figure S14. First-principles calculations for spin Berry curvature. a, b, Spin Berry curvature (Ω_{xy}^z) projected electronic structures and integrated Ω_{xy}^z for Gr/1T-TaS₂ heterostructures with and without CCDW phase. In each panel, green arrows indicate Dirac point of Gr. In a, the inset shows spin Berry curvature hotspots originating from interaction between Dirac and CCDW bands.

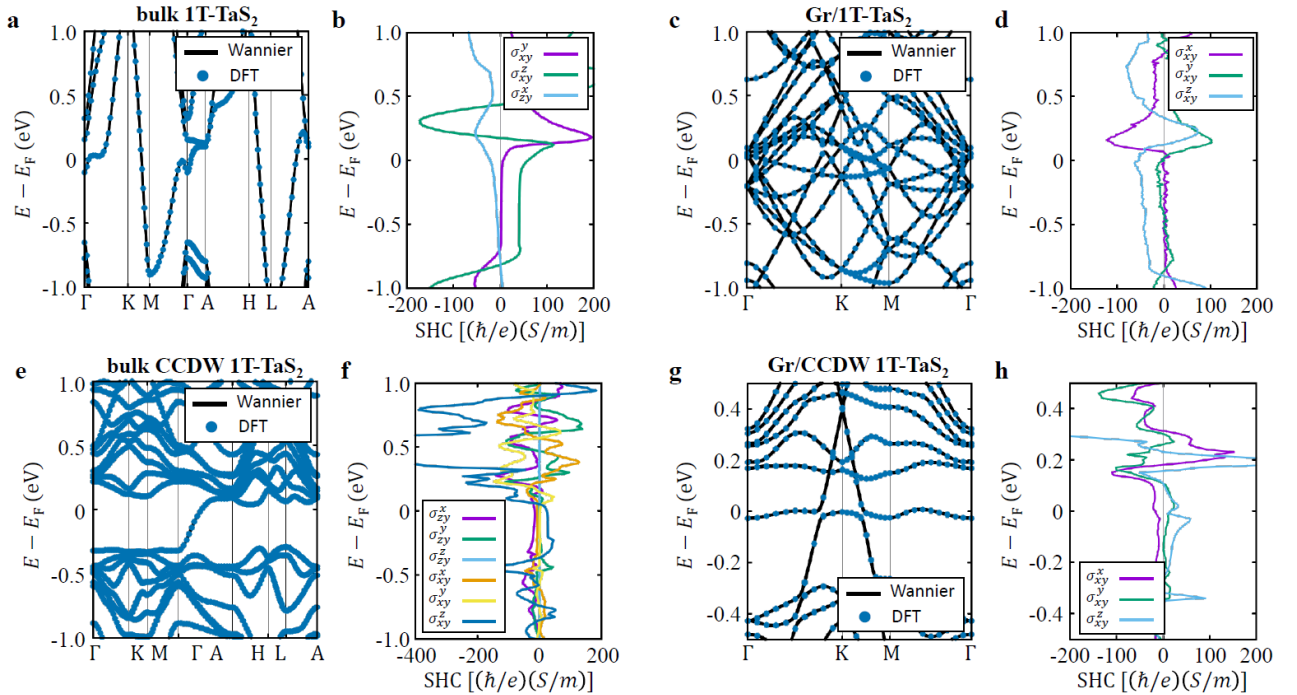


Figure S15. Electronic structure and selected SHC components of bulk normal 1T-TaS₂ (a,b), Gr/normal 1T-TaS₂ heterostructure (c,d), bulk CCDW 1T-TaS₂ (e,f), and Gr/CCDW 1T-TaS₂ heterostructure (g,h). In a, c, e, g, solid black line shows the band structure obtained by Wannier90 showing excellent agreement blue dots obtained from DFT calculations.

a	bulk 1T-TaS ₂	b	Gr/1T-TaS ₂	c	bulk CCDW 1T-TaS ₂	d	Gr/CCDW 1T-TaS ₂
	$\sigma_{ij}^x = \begin{pmatrix} -6.5 & 0 & 0 \\ 0 & 6.5 & 20.6 \\ 0 & -22.0 & 0 \end{pmatrix}$		$\sigma_{ij}^x = \begin{pmatrix} -0.26 & -6.08 \\ 0.16 & < 0 \end{pmatrix}$		$\sigma_{ij}^x = \begin{pmatrix} -2.9 & -8.4 & 4.1 \\ 1.8 & 1.8 & 21.5 \\ -3.3 & -15.7 & < 0.1 \end{pmatrix}$		$\sigma_{ij}^x = \begin{pmatrix} -13.07 & -16.64 \\ -4.62 & 10.01 \end{pmatrix}$
	$\sigma_{ij}^y = \begin{pmatrix} 0 & 6.5 & -20.6 \\ 6.5 & 0 & 0 \\ 22.0 & 0 & 0 \end{pmatrix}$		$\sigma_{ij}^y = \begin{pmatrix} -5.35 & 1.28 \\ 1.97 & 0.60 \end{pmatrix}$		$\sigma_{ij}^y = \begin{pmatrix} -3.2 & 1.8 & -22.0 \\ 2.2 & 2.8 & 3.2 \\ 15.6 & -2.9 & < 0.1 \end{pmatrix}$		$\sigma_{ij}^y = \begin{pmatrix} -14.54 & 16.35 \\ 5.96 & 10.17 \end{pmatrix}$
	$\sigma_{ij}^z = \begin{pmatrix} 0 & 59.6 & 0 \\ -59.6 & 0 & 0 \\ 0 & 0 & 0 \end{pmatrix}$		$\sigma_{ij}^z = \begin{pmatrix} -9.7 & -52.8 \\ 53.7 & -11.58 \end{pmatrix}$		$\sigma_{ij}^z = \begin{pmatrix} 0.4 & 23.0 & 0.3 \\ -24.2 & -0.3 & < 0.1 \\ 0.4 & < 0.1 & -0.1 \end{pmatrix}$		$\sigma_{ij}^z = \begin{pmatrix} 1.83 & 14.70 \\ -22.17 & 2.23 \end{pmatrix}$

Figure S16. Calculated SHC tensor at $E = E_F$ for normal 1T-TaS₂ (a), Gr/normal 1T-TaS₂ heterostructure (b), CCDW 1T-TaS₂ (c), and Gr/CCDW 1T-TaS₂ heterostructure (d), in units of $(\hbar/e)S/cm$. " < 0.1 " indicates that the absolute value of that component is smaller than 0.1 $(\hbar/e)S/cm$.

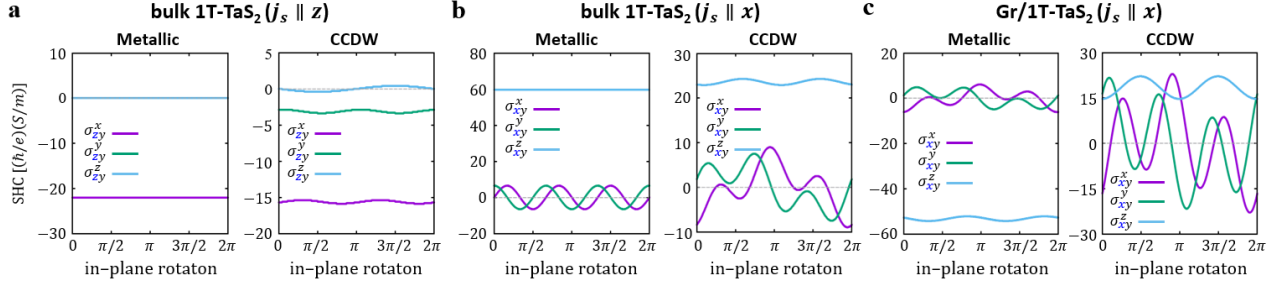


Figure S17. Selected SHC components corresponding to our experimental observation as function of in-plane rotation angle. Here, direction of x at the zero-rotation angle indicates a zigzag direction for the normal 1T-TaS₂, as illustrated in Figure S12 for CCDW 1T-TaS₂.

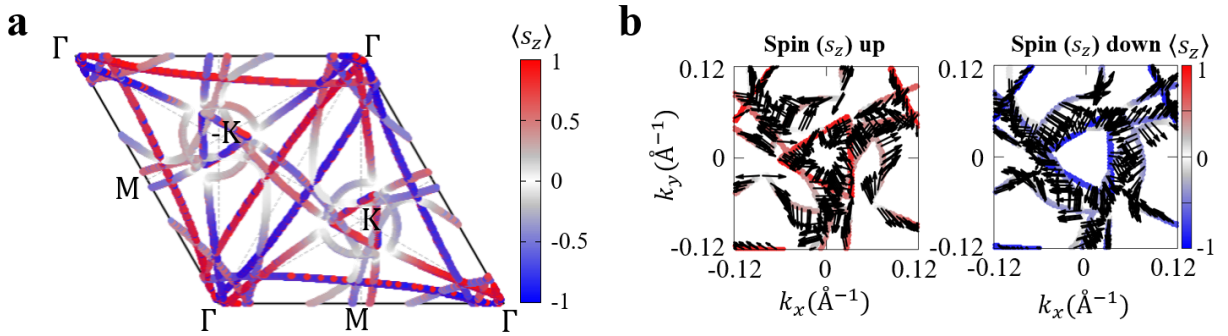


Figure S18. Spin-resolved Fermi surface of Gr/normal 1T-TaS₂ heterostructure (a) and its in-plane spin distribution near K point (b).

References

- [1] M. Yoshida, R. Suzuki, Y. Zhang, M. Nakano and Y. Iwasa, "Memristive phase switching in two-dimensional 1T-TaS₂ crystals," *Science Advances*, vol. 1, p. e1500606, 2015.
- [2] M. Yoshida, T. Gokuden, R. Suzuki, M. Nakano and Y. Iwasa, "Current switching of electronic structures in two-dimensional 1T-TaS₂ crystals," *Physical Review B*, vol. 95, p. 121405(R), 2016.
- [3] Y. Yu, F. Yang, X. F. Lu, Y. J. Yan, Y.-H. Cho, L. Ma, X. Niu, S. Kim, Y.-W. Son, D. Feng, S. Li, S.-W. Cheong, X. H. Chen and Y. Zhang, "Gate-tunable phase transitions in thin flakes of 1T-TaS₂," *Nature Nanotechnology*, vol. 10, pp. 270-276, 2015.
- [4] M. Yoshida, Y. Zhang, J. Ye, R. Suzuki, Y. Imai, S. Kimura, A. Fujiwara and Y. Iwasa, "Controlling charge-density-wave states in nano-thick crystals of 1T-TaS₂," *Scientific Reports*, vol. 4, p. 7302, 2014.
- [5] L. M. Malard, M. A. Pimenta, G. Dresselhaus and M. S. Dresselhaus, "Raman spectroscopy in graphene," *Physics Reports*, vol. 473, pp. 51-87, 2009.
- [6] B. Kim, J. Park, J. Li, H. Lim, G. Myeong, W. Shin, S. Kim, T. Jin, Q. Zhang, K. Sung, K. Watanabe, T. Taniguchi, E. Hwang and S. Cho, "Charge-Density-Wave Proximity Effects in graphene," arXiv:2201.04844.
- [7] W. Yan, E. Sagasta, M. Ribeiro, Y. Niimi, L. E. Hueso and F. Casanova, "Large room temperature spin-to-charge conversion signals in a few-layer graphene/Pt lateral heterostructure," *Nature Communications*, vol. 8, p. 661, 2017.
- [8] C. K. Safeer, J. Ingla-Aynés, F. Herling, J. H. Garcia, M. Vila, N. Ontoso, M. Reyes Calvo, S. Roche, L. E. Hueso and F. Casanova, "Room-Temperature Spin Hall Effect in Graphene/MoS₂ van der Waals Heterostructures," *Nano Letters*, vol. 19, no. 2, pp. 1074-1082, 2019.
- [9] F. Herling, C. K. Safeer, J. Ingla-Aynés, N. Ontoso, L. E. Hueso and F. Casanova, "Gate tunability of highly efficient spin-to-charge conversion by spin Hall effect in graphene proximitized with WSe₂," *APL Materials*, vol. 8, no. 7, p. 071103, 2020.
- [10] A. A. Mostofi et al., "An updated version of wannier90: A tool for obtaining maximally-localised wannier functions," *Computer Physics Communications*, vol. 185, p. 2309–2310, 2017.
- [11] G. Pizzi et al., "Wannier90 as a community code: new features and applications," *Journal of Physics: Condensed Matter*, vol. 32, p. 165902, 2020.
- [12] I. Souza, N. Marzari and D. Vanderbilt, "Maximally localized wannier functions for entangled energy bands," *Physical Review B*, vol. 65, p. 035109, 2001.
- [13] M. Seemann, D. Ködderitzsch, S. Wimmer and H. Ebert, "Symmetry-imposed shape of linear response tensors," *Physical Review B*, vol. 92, p. 155138, 2015.
- [14] W. Yanez, Y. Ou, R. Xiao, J. Koo, J. T. Held, S. Ghosh, J. Rable, T. Pillsbury, E. G. Delgado, K. Yang, J. Chamorro, A. J. Grutter, P. Quarterman, A. Richardella, A. Sengupta, T. McQueen, J. Borchers, K. Andre

Mkhoyan, B. Yan and N. Samarth, "Spin and Charge Interconversion in Dirac-Semimetal Thin Films," *Physical Review Applied*, vol. 16, p. 054031, 2021.